

Analyzing Calcites With In-Situ LA-ICP-MS to Obtain an Age for the McArras Brook
Formation

By

Ben Thompson

Submitted in partial fulfillment of the requirements for the degree of Bachelor of Science in
Earth Sciences

At

Dalhousie University

Halifax, Nova Scotia

April 2025

Supervisor, Dr. Richard Cox

Table of Contents

List of Figures	4
Abstract	7
Acknowledgements	7
Introduction and Motivation	8
Previous Work	9
Geological Setting	10
Methods	11
Results	12
Discussion	31
Conclusion	33
References	34
Appendices	36
Appendix A – REE Data	36
Appendix B – Iolite Data Table Export	37
Appendix C – Select REE Concentration Images	43

List of Figures

Fig. 1 A summary geological map of Nova Scotia, showing off the study area and surrounding geology.

Incident Light Photos

Fig. 2 An incident light photograph of sample 1a, with ablation site highlighted in red for ease of distinction.

Fig. 3 An incident light photograph of sample 1b, with ablation sites highlighted in red for ease of distinction.

Fig. 4 An incident light photograph of sample 1d, with ablation sites highlighted in red for ease of distinction.

Fig. 5 An incident light photograph of sample 3a, with ablation site highlighted in red for ease of distinction.

Collages of Isotope Data Overlaying Incident Light Photographs for Ablation Site Context

Fig. 6 Collage of isotope data from the ablation site for sample 1a.

Fig. 7 Collage of isotope data from ablation sites for sample 1b.

Fig. 8 Collage of isotope data from the upper ablation site for sample 1d.

Fig. 9 Collage of isotope data from the lower ablation site for sample 1d.

Fig. 10 Collage of isotope data from ablation sites for sample 3a.

Isotope Maps Exported from Iolite V4

Fig. 11 Isotope maps of concentration of ^{24}Mg , ^{55}Mn , Total Pb, and ^{238}U for sample 1a.

Fig. 12 Isotope maps of concentration of ^{24}Mg , ^{55}Mn , Total Pb, and ^{238}U for the left site on sample 1b.

Fig. 13 Isotope maps of concentration of ^{24}Mg , ^{55}Mn , Total Pb, and ^{238}U for the right site on sample 1b.

Fig. 14 Isotope maps of concentration of ^{24}Mg , ^{55}Mn , Total Pb, and ^{238}U for the top site on sample 1d.

Fig. 15 Isotope maps of concentration of ^{24}Mg , ^{55}Mn , Total Pb, and ^{238}U for the bottom site on sample 1d.

Fig. 16 Isotope maps of concentration of ^{24}Mg , ^{55}Mn , Total Pb, and ^{238}U for sample 3a.

REE Trend Graphs

Fig. 17 REE trend graph for sample 1a, showing difference across different sections of the ablation site.

Fig. 18 REE trend graph for the left ablation site on sample 1b, showing difference across different sections of the ablation site.

Fig. 19 REE trend graph for the right ablation site on sample 1b, showing difference across different sections of the ablation site.

Fig. 20 REE trend graph for sample 1d, only one section is shown because of data errors.

Fig. 21 REE trend graph for sample 3a, the vein sample, showing difference across different sections of the ablation site within just the calcite and also including the surrounding basalt.

Other Isotope Graphs

Fig. 22 Three plots, Ce, Yb, and Ce/Yb, to visualize LREEs vs HREEs throughout samples.

Fig. 23 Three plots, Sr, Ba, and Sr/Ba to visualize a proxy for growth speed.

Fig. 24 Two plots, ^{206}Pb , and ^{238}U to visualize concentrations of each.

Fig. 25 Two plots, both $^{206}\text{Pb}/^{238}\text{U}$, to visualize the ratio between them. One plot is with, and one without, the bottom site of sample 1d.

Fig. 26 Two plots, both Mg concentrations across samples. One graph uses a linear scale and the other uses a log scale because of some relatively extreme values.

Abstract

The McArras Brook Formation is located on the Northwest coast of Nova Scotia, Canada, consists of interlayered red-bed sedimentary rocks, and amygdaloidal basalt. This formation plays a part in Dalhousie University's intermediate field school course each Summer, however other than this it has not been often studied. The formation has been placed stratigraphically in the early Devonian period, but no absolute (numerical) age is known, nor are there absolute ages known for surrounding units.

The amygdaloidal basalts in the unit contain calcite, forming the amygdules, which has been dated using U-Pb techniques previously for both eruption/volcanism and tectonic events for basalt. The basalts in this unit have also been characterized previously in a Dalhousie project, and this project aims to continue work done on this unit.

This project uses Laser Ablation Inductively Coupled Mass Spectrometry (LA-ICP-MS) to analyze over thirty isotopes in-situ on calcite samples taken from the McArras Brook basalt. Data acquired from analysis is used to image isotopic distribution on sampled locations, to create temperature maps of sampled locations, and ultimately to plot U and Pb ratios to obtain an absolute age for the unit.

Keywords: Calcite dating; Carbonate dating; LA-ICP-MS; U-Pb geochronology; McArras Brook Formation

Acknowledgements

I would like to thank all those who provided support for the project. Primarily Dr. Richard Cox, the supervisor for the project, who was very helpful in providing information and guidance. I would also like to thank Kathleen Clark, and Roman Kislitsyn for their help with LA-ICP-MS hardware usage, and an extra thanks to Kathleen Clark for guidance on software usage and troubleshooting. An extended gratitude to Ingrid Helmke as well for her 2024 project, which this project is a continuation of. Finally, I would like to thank Dr. Tarah Wright, the Dalhousie Earth and Environmental Sciences honours coordinator, who has

helped shape this project and others for the Department of Earth and Environmental Sciences.

Introduction and Motivation

This study is concerned with acquiring an absolute age for the McArras Brook Formation, by using calcites found in amygdules within basalts that make up part of the formation. This will be accomplished using U-Pb dating methods for carbonate minerals using LA-ICP-MS (laser ablation inductively coupled plasma mass spectrometry, often referred to as simply “laser ablation”) for data acquisition. This study builds on work done by I. Helmke in Helmke 2024⁶, which involved characterization of the calcites. The same samples are being used to acquire an age for the formation.

Calcite in the amygdaloidal basalt can be used as a good dating mineral as these crystals would have grown shortly after the eruption of the basalt. Air pockets in the lava flow form vesicles as the lava cools, and calcite precipitates in these vesicles, making them amygdules. This growth time adjacency to the eruption, as well as their size and ease of use as samples, is what makes them a good material to date. With more traditional dating mineral choices, like zircon, absent from this formation, calcite becomes the choice for dating analysis, as in Andjic et al., 2022⁴, and Rembe et al., 2022⁵, which were inspirations for this project. Some cooling history can be recorded and analyzed from data gathered from these crystals as well.

The McArras Brook Formation, located in Northwest Nova Scotia along the Antigonish coast, is the site for Dalhousie’s 3rd year field school during the Summer. Work done to gather an absolute age for this formation can aid in the further education of Earth and Environmental Science students who take this course.

Motivation for this project comes from inspiration from previous calcite U-Pb chronology, with LA-ICP-MS being used to analyze calcites in other studies. These calcites were able to yield ages for basalt formation in different structures. Motivation also comes from a desire to continue work started in Helmke 2024⁶, which began the project by qualifying calcite present in amygdaloidal basalt in the McArras Brook Formation in Antigonish, Nova Scotia.

This project aims to continue that work by obtaining trace element and REE (rare Earth element) data from the same samples, ultimately to obtain an age of eruption for the basalt present in the formation (effectively yielding an absolute age for the formation).

Previous Work

As stated, this project is a continuation of Helmke 2024⁶, and samples are the same throughout the two projects. Considerable analysis was done in Helmke 2024⁶ using UV fluorescence techniques, as well as scanning electron microscope (SEM) work done at Saint Mary's University. Major element data was collected using the SEM, and Back Scattering Electron (BSE) images were made of the samples. This analysis allowed the calcite samples to be qualified for their general composition. The samples contain both calcite and dolomite, as well as some quartz and ankerite, and clear zoning can be seen on some samples⁵. It was determined that there were likely two growth events for the calcite amygdules, at ~250°C and ~375°C⁶. These two growth events could be interpreted as a post-eruption growth, and a subsequent growth event during the Acadian Orogeny⁶.

Recent calcite dating work includes Andjic et al. 2022⁴ and Rembe et al. 2022⁵, which were both inspirations for this project and the previous project, Helmke 2024⁶. LA-ICP-MS analysis was done on calcites in amygdaloidal basalts in both papers, using U and Pb data from analysis to determine an age for their respective structures.

Geological Setting

Nova Scotia has a diverse Geological history including areas like the McArras Brook. The McArras Brook is located in Northwest Nova Scotia, in the Antigonish Highlands, sandwiched between the Martin's Road Formation and the Knoydart Formation. The formation is part of the Arisaig Group, and is underlain by the Avalon terrain, and there is a disconformity between the McArras Brook Formation and the Ardeness Formation³, which is a calcareous unit. McArras Brook consists of interlayered red-bed sedimentary strata, and basalt flows³. The basalt in the McArras Brook contains calcite amygdules, which would typically form shortly after eruption/volcanism, and form the main focus for this project. It is thought that the pull-apart basin during nearby orogenic events caused the basalt spreading centers³, giving a reason for the basalt presence in the McArras Brook Formation, and that the formation was subject to alteration during the Acadian Orogeny.

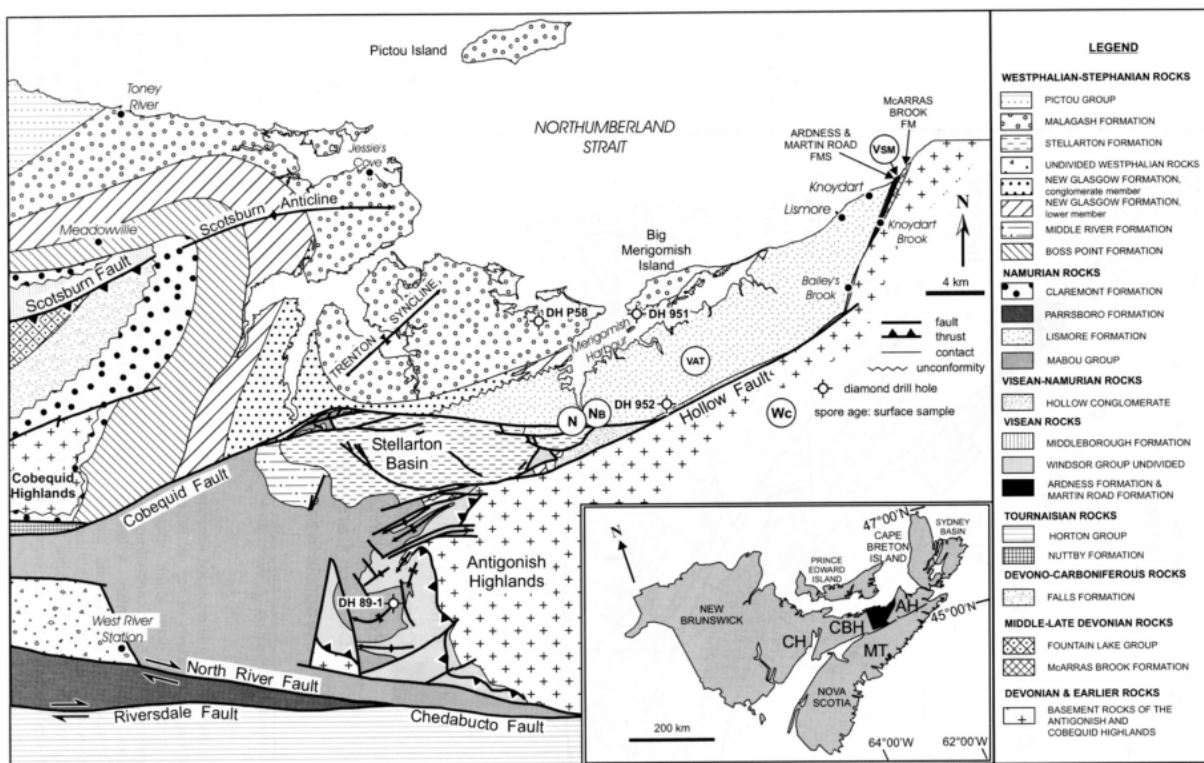


Fig. 1 A geological map showing the Antigonish Highlands coast, including the McArras Brook Formation, (J.B. Murphy et al., 2006)².

Methods

For analysis, samples were cut, mounted in epoxy resin, and polished. This work was done previously, as stated in the introduction, for Helmke 2024 by I. Helmke.

Before chemical data was collected, visual maps of the samples were made using an incident light visual binocular microscope, with an AmScope LED-56S LED ring light attachment for illumination, connected with an AmScope eye piece camera, model MD500L, to AmScope software to capture and stitch together images of the samples. All images of the samples included in this project were taken at 1.6x magnification. This was to create maps for orientation as to where analysis was being done on the samples when plotting points for the laser. The samples were all re-imaged using the same parameters and software/hardware to pinpoint ablation sites on each sample after laser analysis was done (see figures 2-5).

For laser analysis, samples 1a, 1b, 1d, and 3a were placed into the stage for the laser, along with MACS-1 and MACS-3 standard powders pressed into pucks. The laser used was a 213nm laser feeding into a Thermo iCAP Q quadrupole mass spectrometer. For a carrier gas, He was used with a flow rate of 900ml/minute. During analysis, laser fluence was between 4.5 - 5.2J/cm². MACS-1 and MACS-3 powders were analyzed first, with two lines of five passes, a scan speed of 20µm, a depth/pass of 0µm, an output of 25%, a laser frequency of 10Hz, and a spot size of 25µm. Collected data from the MACS powders was repeated between each sample analysis. All samples were analyzed with a raster pattern broken into lines with a raster spacing of 20µm, one pass, 0µm depth setting, 20µm scan speed, 25% output, 10Hz frequency, and a 20µm spot size.

The isotopes included in the scan were ²⁴Mg, ³¹P, ⁴³Ca, ⁵⁵Mn, ⁵⁷Fe, ⁶³Cu, ⁶⁵Cu, ⁶⁶Zn, ⁷⁵As, ⁸⁵Rb, ⁸⁸Sr, ⁸⁹Y, ¹³³Cs, ¹³⁷Ba, REEs without isotopes of Pm and Tb, ²⁰⁴Pb, ²⁰⁶Pb, ²⁰⁷Pb, ²⁰⁸Pb, ²³²Th, and ²³⁸U.

Data obtained from laser ablation was reduced using Iolite V4 software^{9, 10}, following the guide by Kathleen Clark available in the Dalhousie LA-ICP-MS laboratory. Iolite was also used for creating element trace maps for the samples, and for reducing and compiling the

data acquired from the laser analysis into useable and interpretable formats. Data files were separated between ablation dates (March 3rd and 4th), with compiled laser logs (using the log compiler feature on Lolite) were separated the same way. References and samples were separated into their own selections with a start crop value of 20 and an end crop value of 15. The baseline group was created from the autoselect tool, setting the parameters as less than 10 0000, and selecting all. Internal reference used was ^{43}Ca , with a weight percent value of 38. For imaging, height and width varied depending on the dimensions of the ablation sites, the gradient used was “Polar”, the lower limit was set to 0 and the upper limit was set to “percentile95”. Data from Lolite was then exported and used in Microsoft Excel to normalize and create graphs of Rare Earth Element trends (figures 17-21). For normalization, REEs were normalized vs chondrites with values from Anders and Grevesse (1989)¹.

Paint.net software was also used for minor image processing and modification, including adding highlighted boxes on ablation sites for visual ease, and creating image collages of data overlying ablation sites.

Results

Where ablation sites ended up were not in the exact intended locations, as this was my first time using the software and hardware for LA-ICP-MS. Data acquired, however, was still quite usable for all samples. Ablation sites were also easily pinpointed with the naked eye on the samples, as well as with an incident light visual microscope (as seen in figures 2-5), although some sites were harder to see than others, for this reason all sites have been highlighted in red. Mg, Mn, total Pb (combination of ^{204}Pb , ^{206}Pb , ^{207}Pb , ^{208}Pb), and ^{238}U data exported from Lolite has been transposed overtop of sections of the sample photos to put selections in context, in sample 1d ^{238}U has been omitted for the second site (bottom of figure 4), as there seemed to be an error in the line scans for the ^{238}U channel. In the full images of these isotopes (figures 11-16) the scale bar and colour scale can be seen as

well, with blue being lowest and yellow being highest in concentration, and absolute values differing across each isotope (values visible on individual scales).

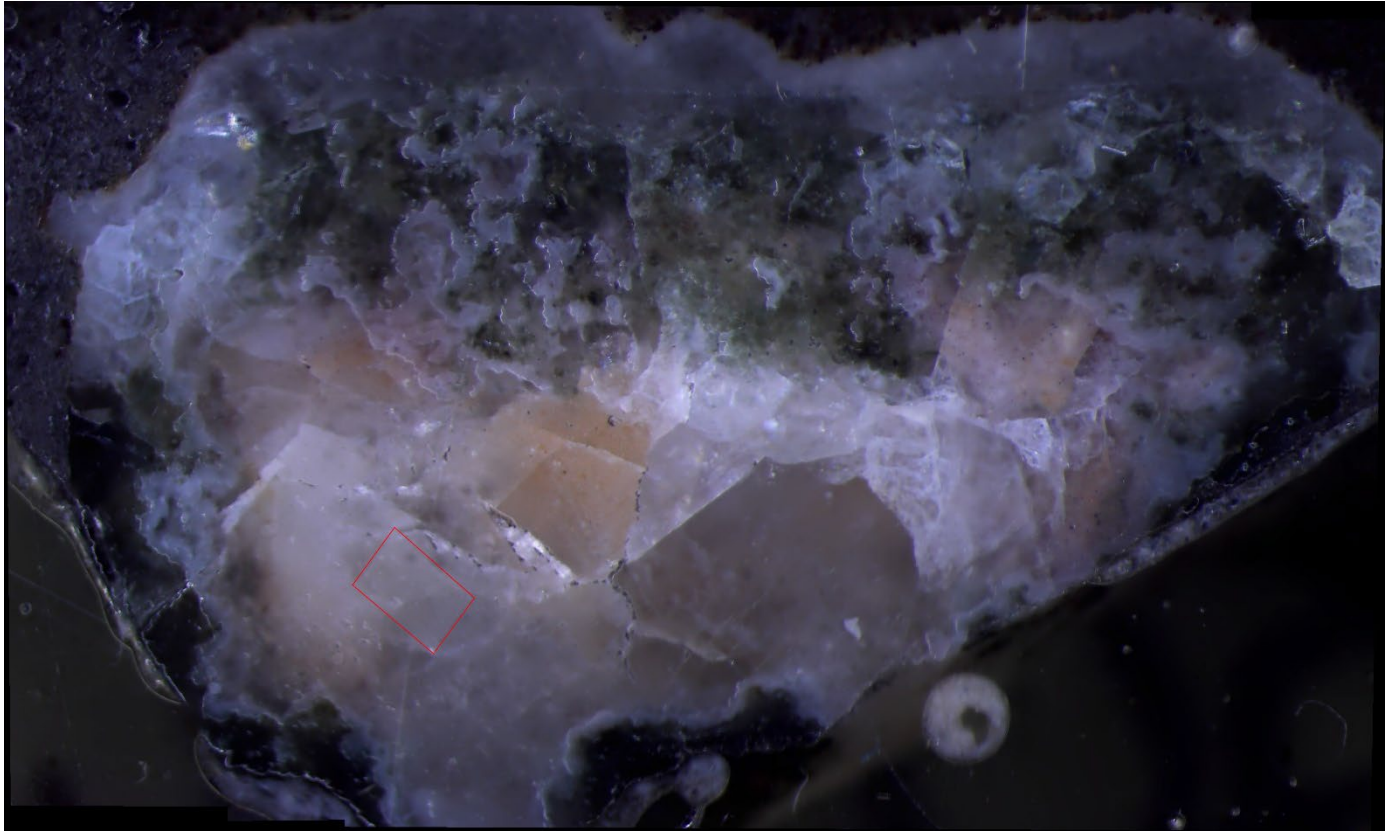


Fig. 2 Sample 1a post ablation, with the ablation site marked in red. Ablation was done in a large section of white/clear calcite (Ben Thompson).

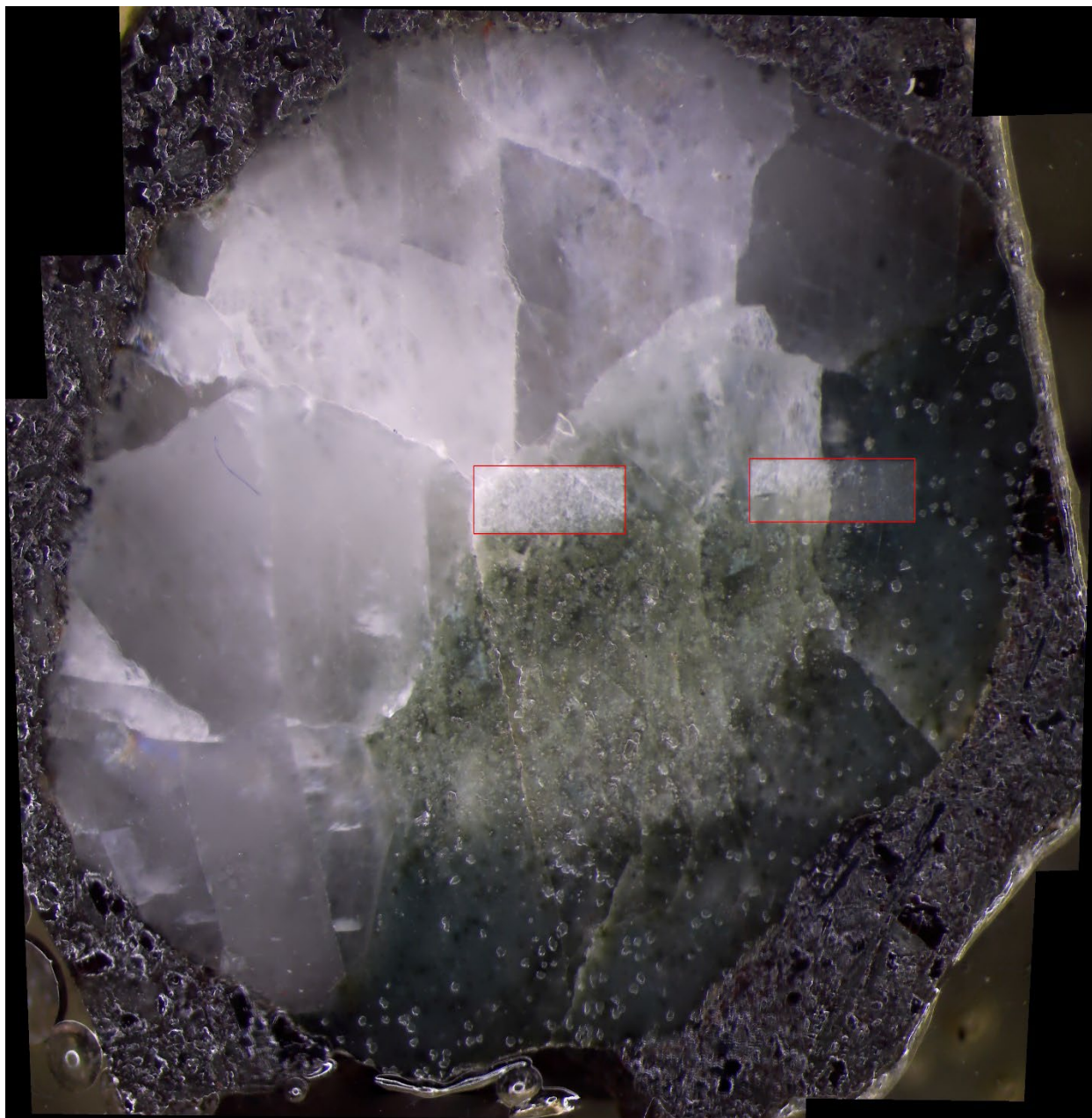


Fig. 3 Sample 1b post ablation with ablation sites marked in red. Two sites were ablated on sample 1b, one on the edge of the clear/white and green calcite boundary (site 1, left), and one within the green calcite (site 2, right) (Ben Thompson).

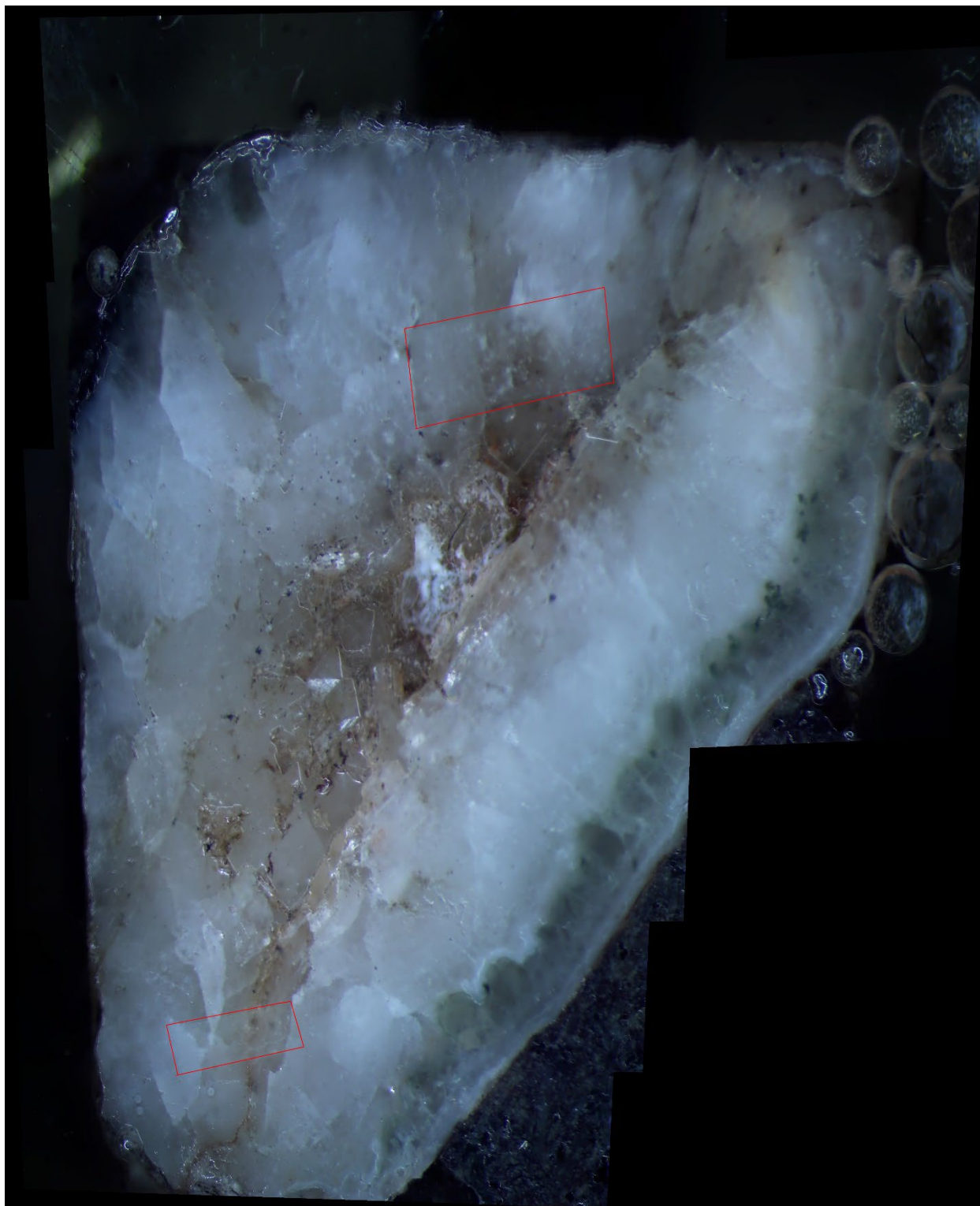


Fig. 4 Sample 1d post ablation with ablation sites marked in red. Two sites were ablated on sample 1d, encompassing both the outer white/clear calcite and the inner growth section of the amygdule (Ben Thompson).

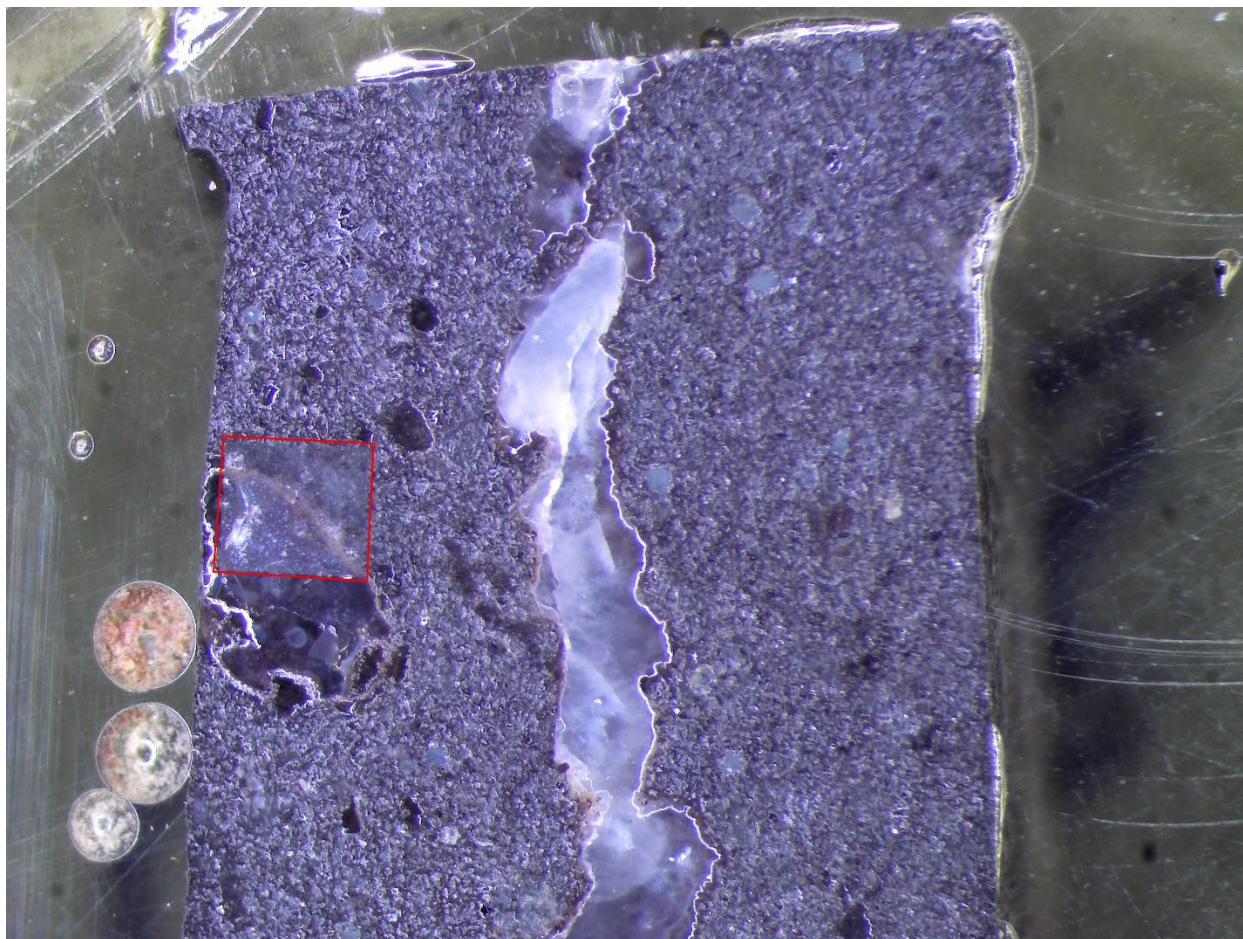
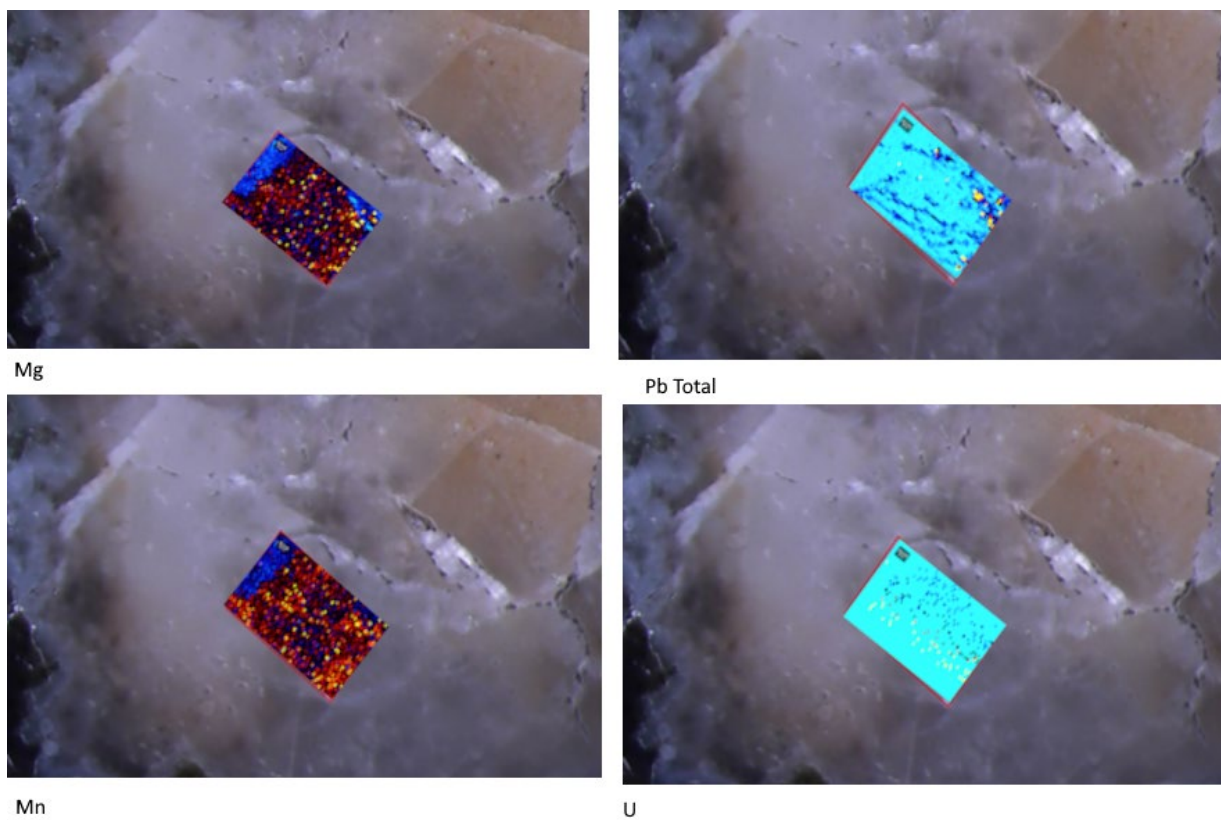
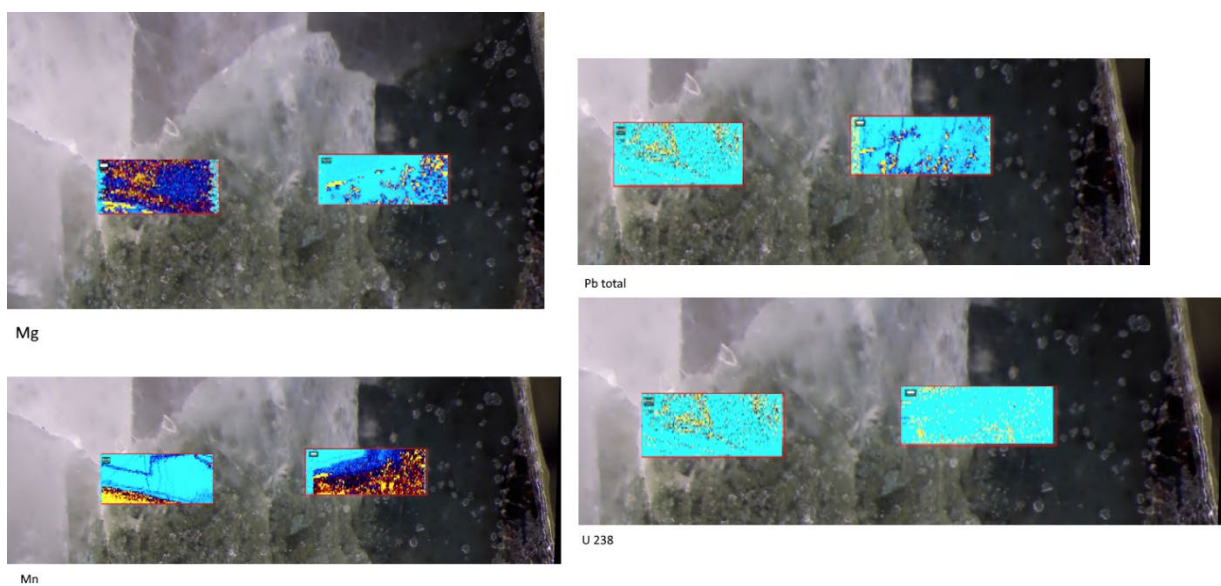


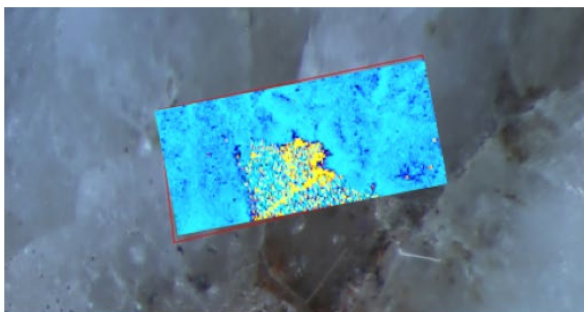
Fig. 5 Sample 3a post ablation with ablation site marked in red. The ablation site encompasses both a section of calcite, and the surrounding basalt. Sample 3a is a vein, rather than an amygdale (Ben Thompson).



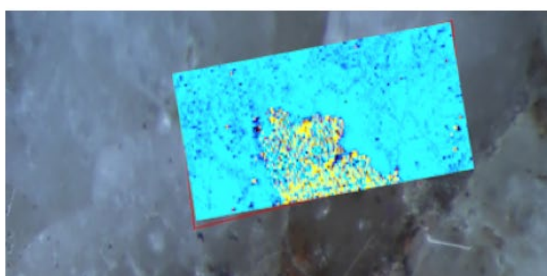
(Fig. 6) Collage of ^{24}Mg , ^{55}Mn , Total Pb, and ^{238}U for sample 1a, showing context for the ablation site.



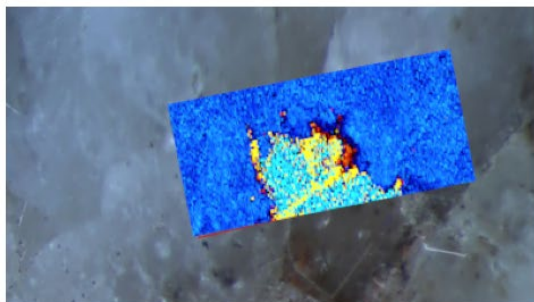
(Fig. 7) Collage of ^{24}Mg , ^{55}Mn , Total Pb, and ^{238}U for both sites on sample 1b, showing context for ablation sites.



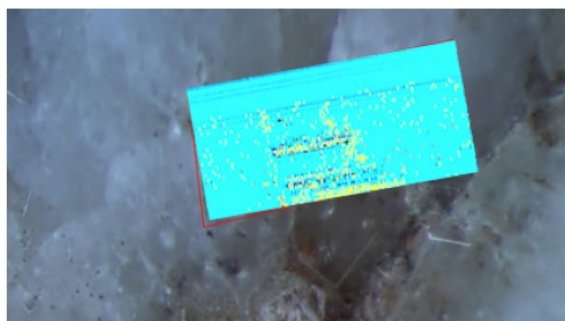
Mg



Pb Total

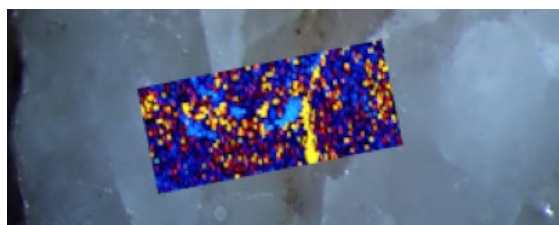


Mn

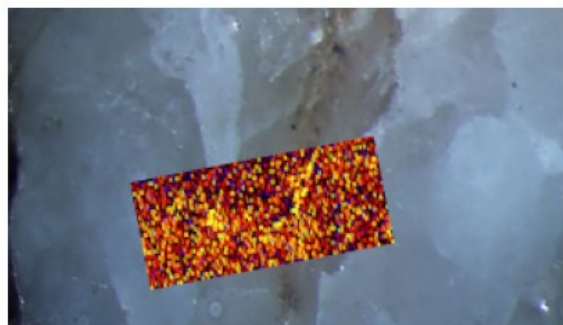


U

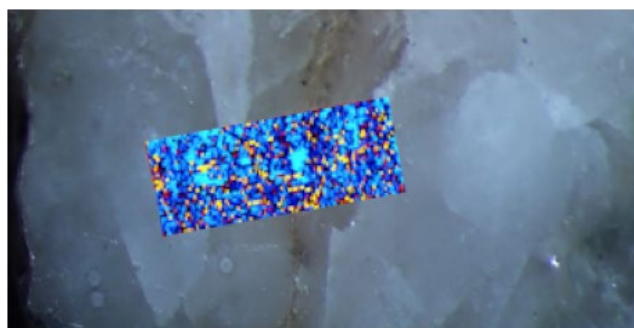
(Fig. 8) Collage showing ^{24}Mg , ^{55}Mn , Total Pb, and ^{238}U for the top site on sample 1d, showing context for ablation sites.



Mg



Mn



Pb total

(Fig. 9) Collage of ^{24}Mg , ^{55}Mn , and Total Pb for the lower site of sample 1d, omitting ^{238}U as there seemed to be an error in the channel.

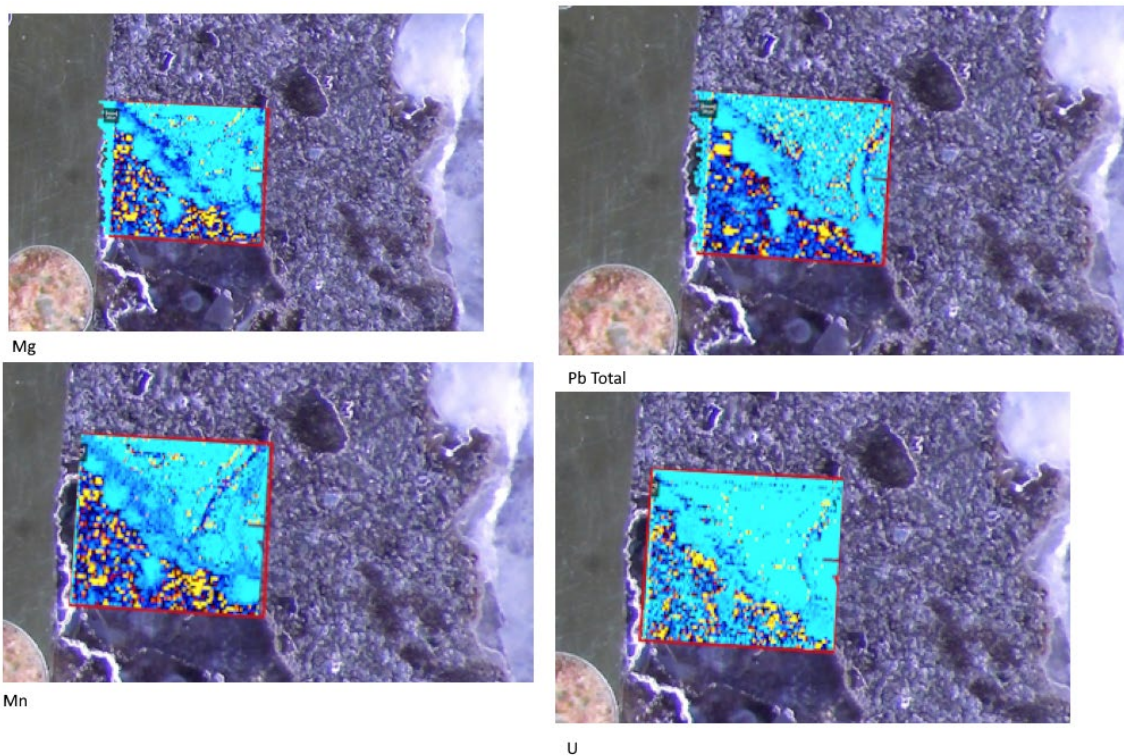


(Fig. 10) Collage of ^{24}Mg , ^{55}Mn , Total Pb, and ^{238}U for sample 3a, showing context for the ablation site.

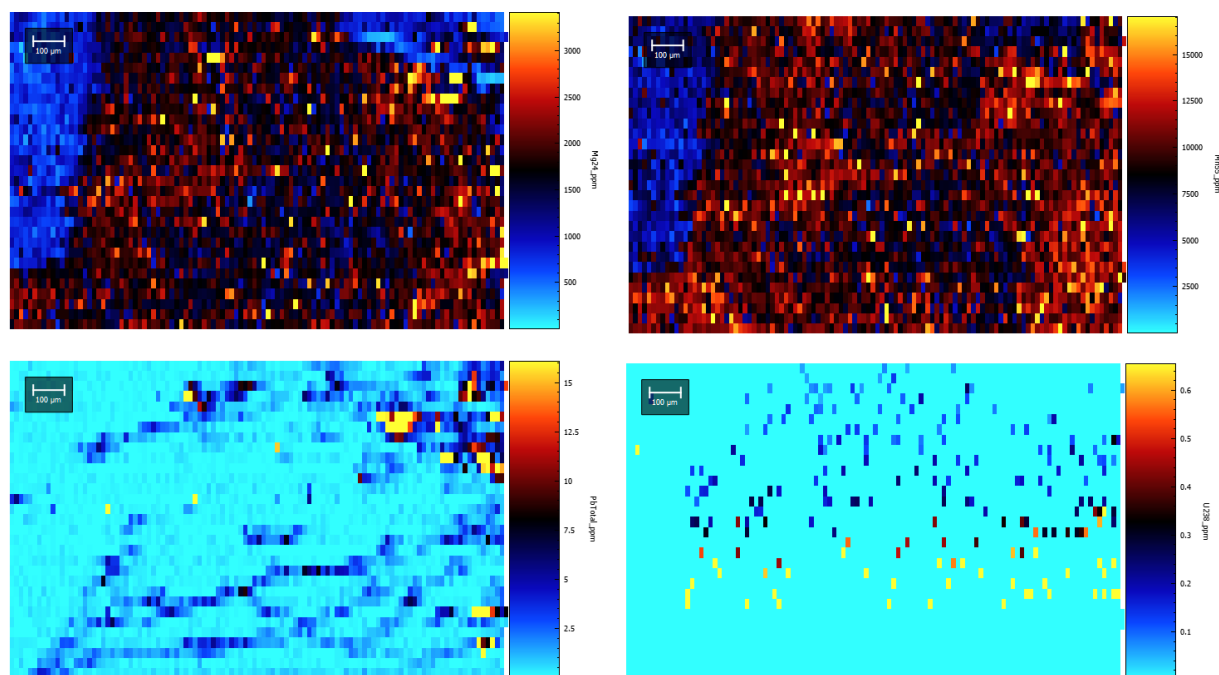


(Fig. 11) ^{24}Mg , ^{55}Mn , Total Pb, and ^{238}U data with scale from sample 1a.

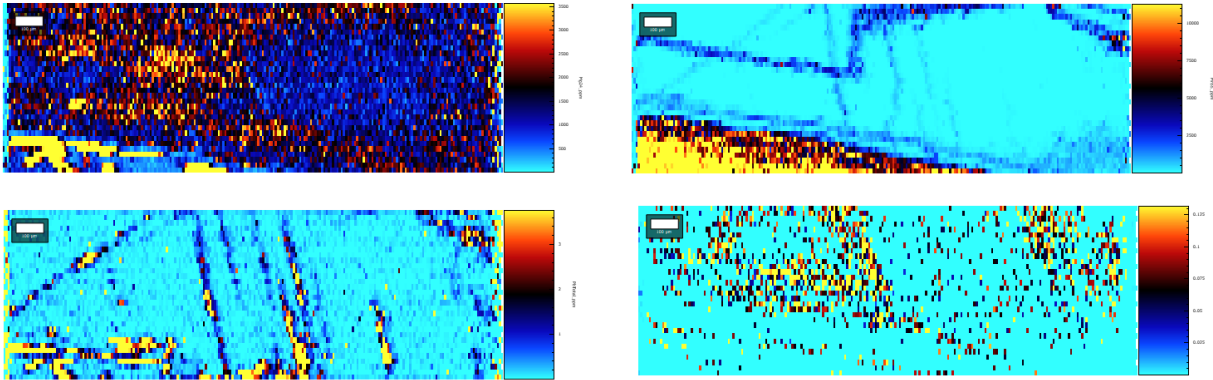


(Fig. 12) ^{24}Mg , ^{55}Mn , Total Pb, and ^{238}U data with scale from the left site of sample 1b.

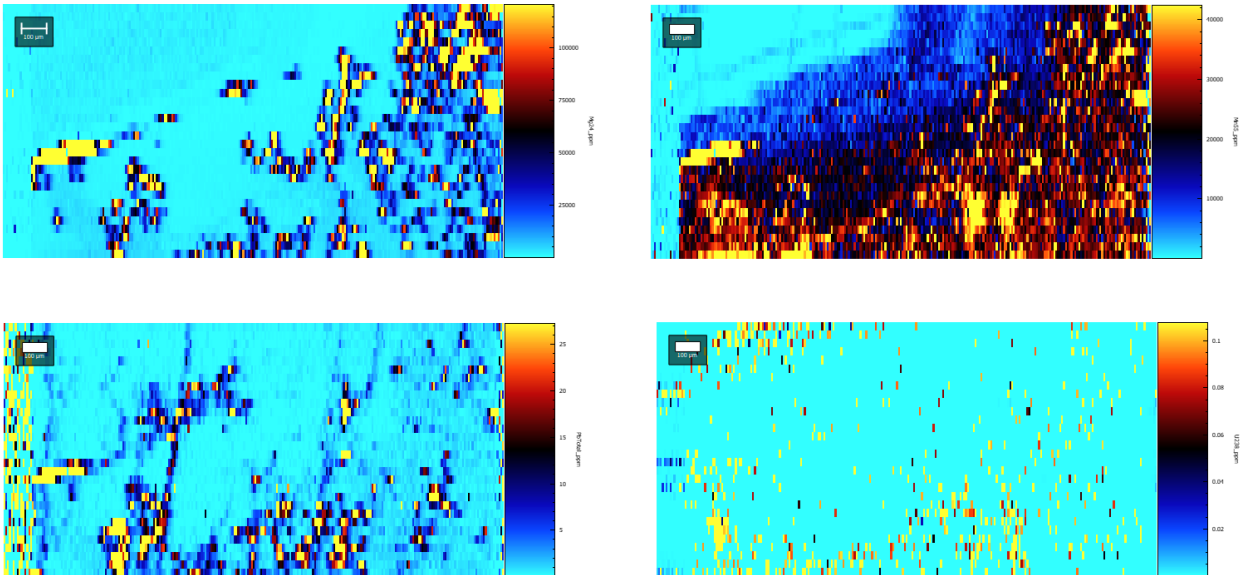


(Fig. 13) ^{24}Mg , ^{55}Mn , Total Pb, and ^{238}U data from the right site of sample 1b.

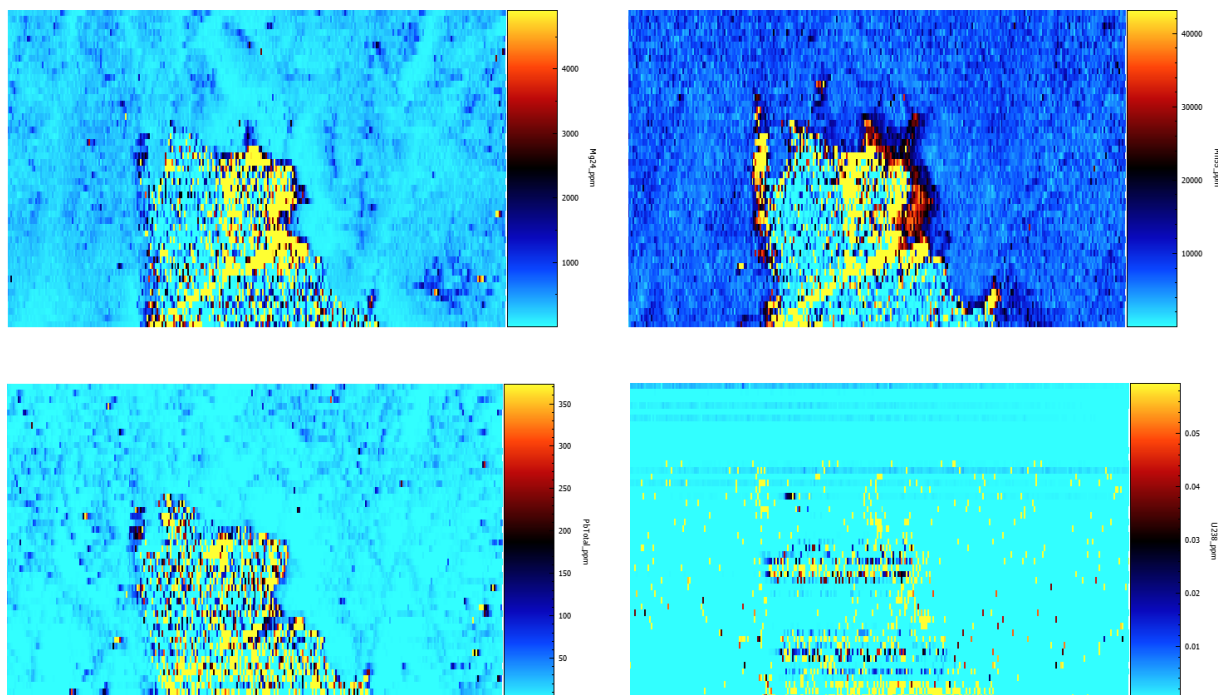


(Fig. 14) ^{24}Mg , ^{55}Mn , Total Pb , and ^{238}U data from the top site of sample 1d.

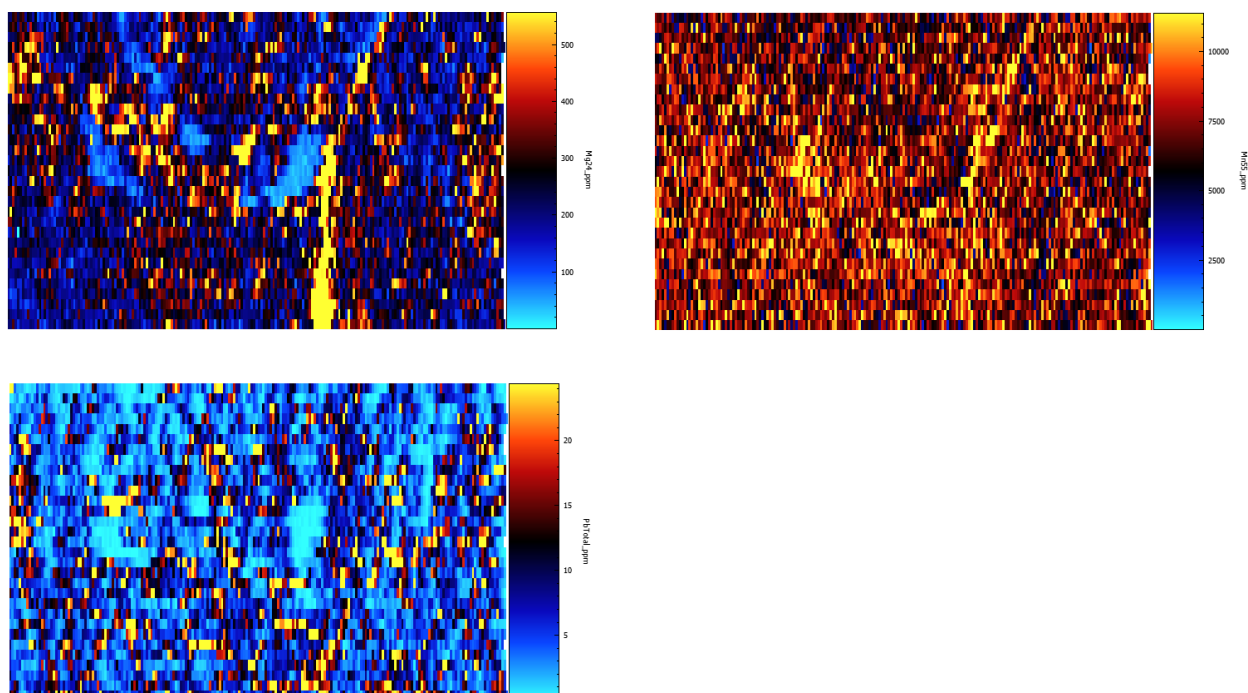


(Fig. 15) ^{24}Mg , ^{55}Mn , and Total Pb from the bottom site of sample 1d, ^{238}U omitted because of channel errors.

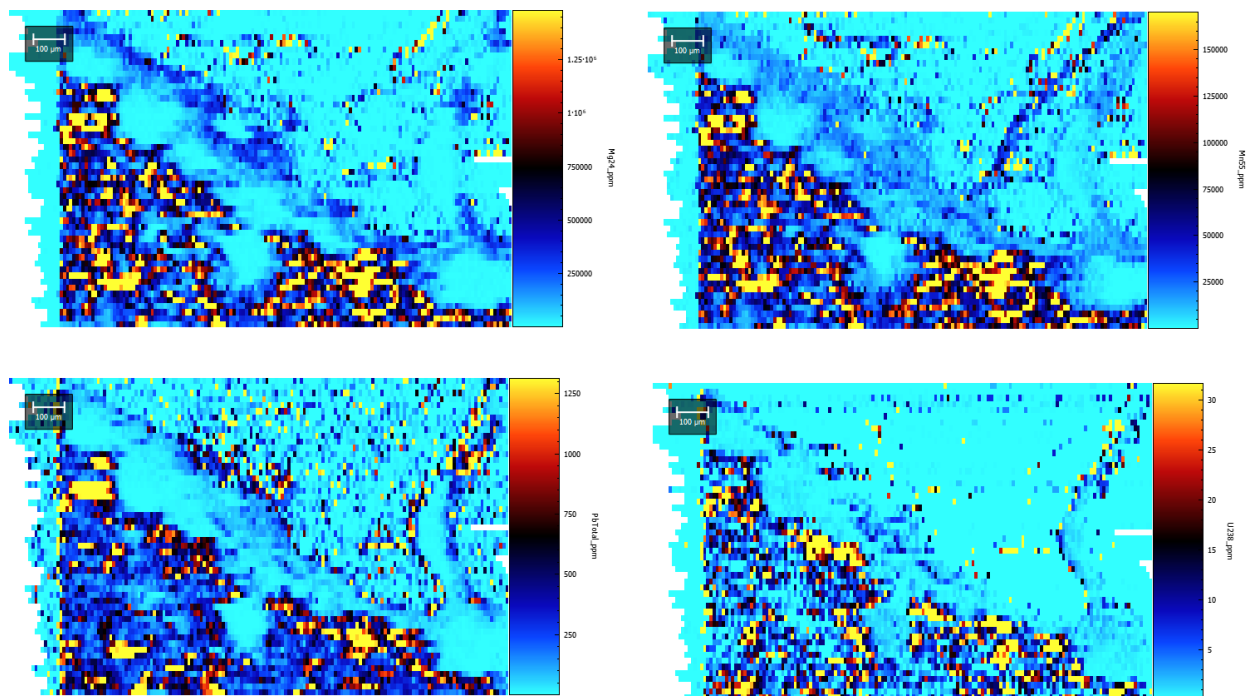


(Fig. 16) ^{24}Mg , ^{55}Mn , Total Pb, and ^{238}U data from sample 3a. Jagged pale blue lines on the left side of these images can be ignored for the most part, as this is due to an error in line-length similarity when calculations were done in Iolite.

Figures 11 to 16 are concentration maps in ppm of ^{24}Mg , ^{55}Mn , Total Pb, and ^{238}U for all of the ablation sites. In general, light blue concentrations are the lowest and yellow concentrations are the highest, all concentrations are relative to the ablation site they are found in, and to the specific isotope channel. In sample 1d, it seems that the ^{238}U channel was corrupted, and this is a possibility for other samples as well, although the exact patterns visible in sample 1d's ^{238}U channel are not visible in other samples.

In figure 11 we can see the data from sample 1a, and there is a much greater difference in concentration for displayed isotopes in the center of the ablation site than on the edges. All of the ^{238}U visible on the site for sample 1a also seems to be in this center area, as the

surrounding concentration is near 0. Some lined patterns can also be seen in the Total Pb image, although they do not seem to correlate directly with U.

In figure 12 is data from sample 1b, specifically the left ablation site (left and right sites can be seen in figure 3), there is a difference in concentration of Mn on the bottom left section of the site, being much higher in Mn, and just above this can be seen an area of high Mg and U concentrations. This upper area also seems to have a relatively lower concentration of Pb.

In figure 13 we can see the data from the right site on sample 1b where there is a gradient of concentration increasing in Mn from left to right and from top to bottom. The other reported isotopes here seem to be concentrated within the higher Mn area, however within these the distribution is somewhat non-uniform. U also seems to have no uniformity on this site.

In figure 14 the data from the top site of sample 1d can be seen, and there is a large central section with much different distribution than the outer section. Looking at figure 4, one can see that this different section is part of the inner growth of sample 1d⁵, which has much higher Mn.

Figure 15 is the lower site for sample 1d, however there is no discernable pattern to the distribution throughout most of the site, other than one line of higher concentrations through Mg and Mn on the middle right section of the site.

Figure 16 is from sample 3a, which is a vein rather than an amygdale. The difference between the calcite vein and the surrounding basalt can be seen nicely in these images. A rim of very low concentration can also be seen between the inner part of the calcite and the basalt, with a line of moderate concentration separating the rim and the basalt.

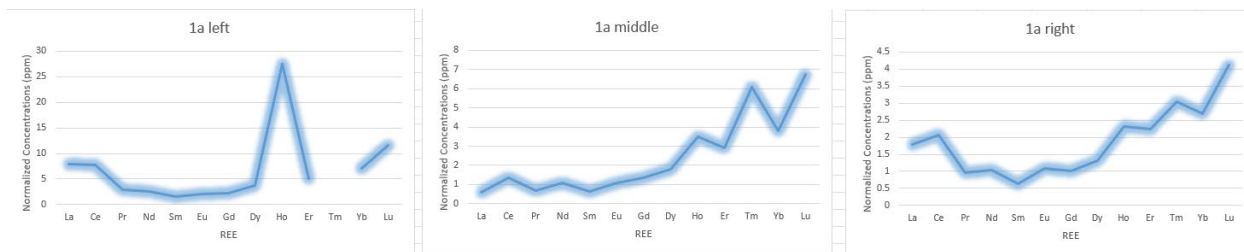


Fig. 17 Excel REE plots for sample 1a, separated into zones of interest. The graphs show the line of the values, and an error cloud around them.

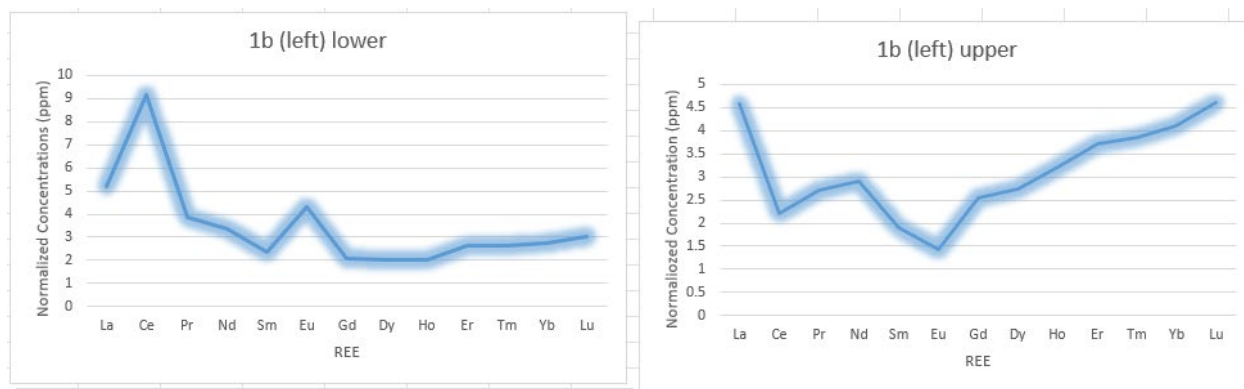


Fig. 18 Excel REE plots for the left site on sample 1b, separated into zones of interest. The graphs show the line of the values, and an error cloud around them.

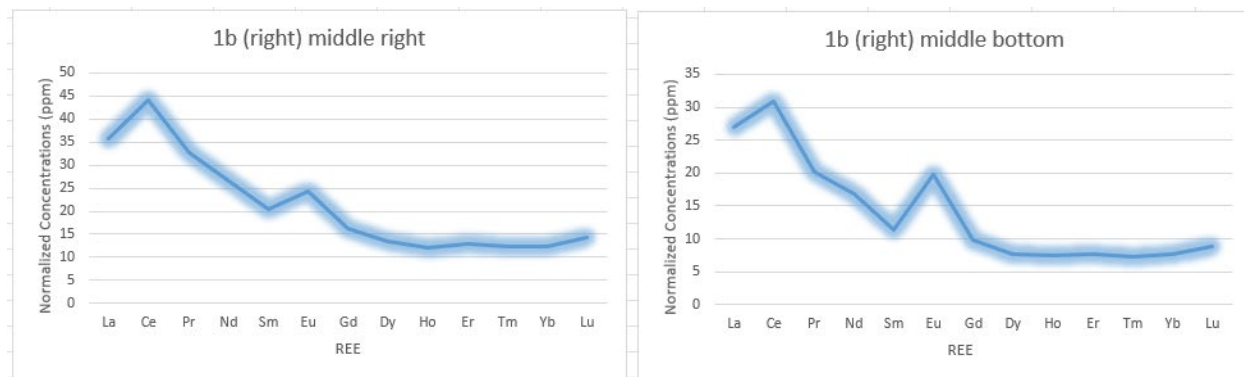


Fig. 19 Excel REE plots for the right site on sample 1b, separated into zones of interest. The graphs show the line of the values, and an error cloud around them.

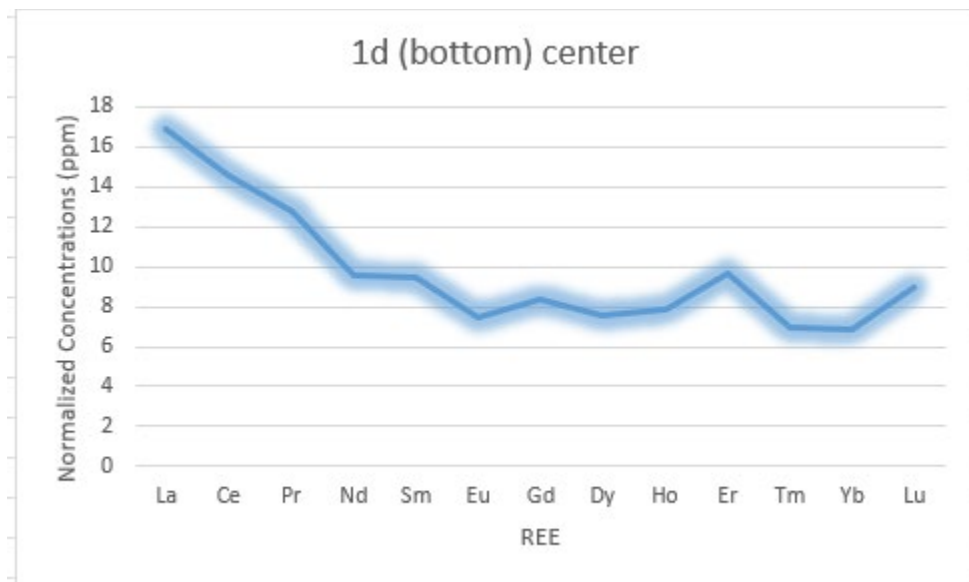


Fig. 20 Excel REE plot for the bottom site of sample 1d. Most REE data acquired from sample 1d was unusable and thus missing (as seen in figure II in Appendix A). The graph shows the line of the values, and an error cloud around them.

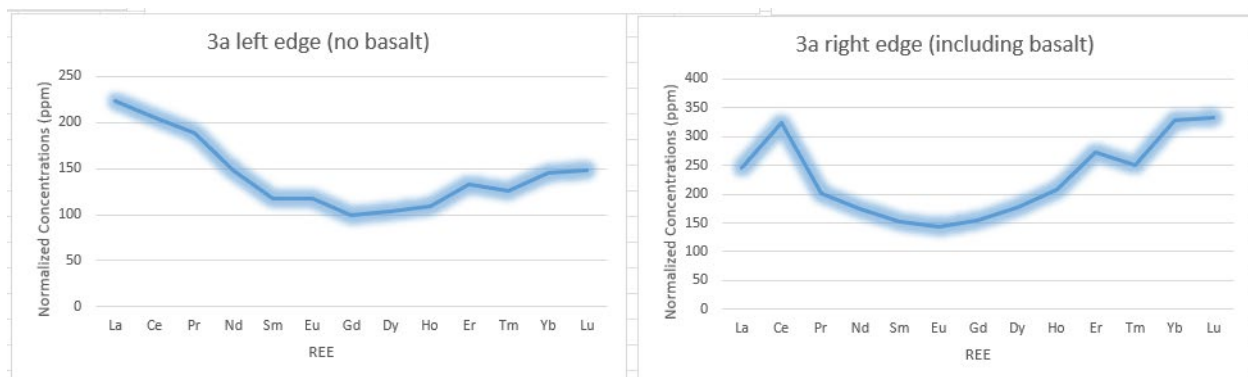


Fig. 21 Excel REE plot for sample 3a, separated into zones of interest, with one zone being wholly within the calcite crystal, and one zone encompassing part of the surrounding basalt. The graphs show the line of the values, and an error cloud around them.

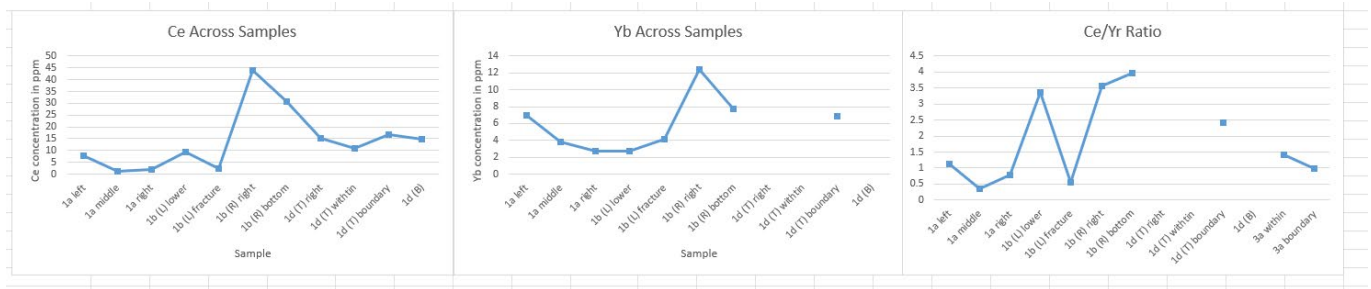


Fig. 22 Plots of Ce and Yb across all samples (except sample 3a, which had extremely dissimilar values), and Ce/Yb ratio for all samples.

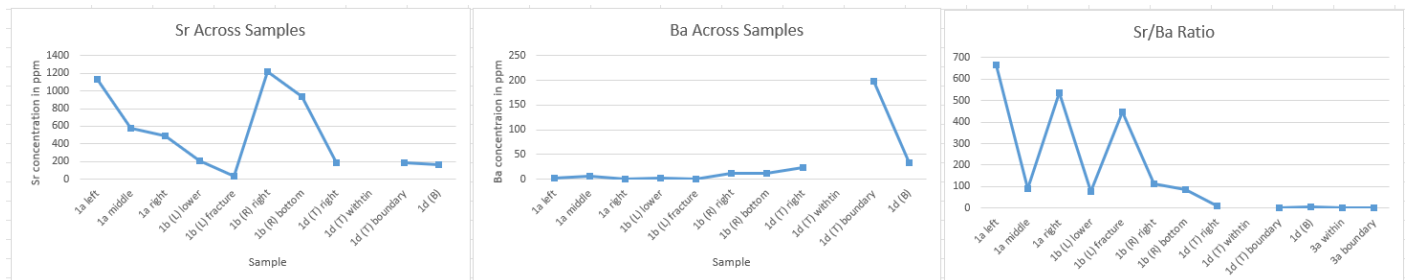


Fig. 23 Plots of Sr and Ba across all samples (except sample 3a, which had extremely dissimilar values), and Sr/Ba ratio for all samples.

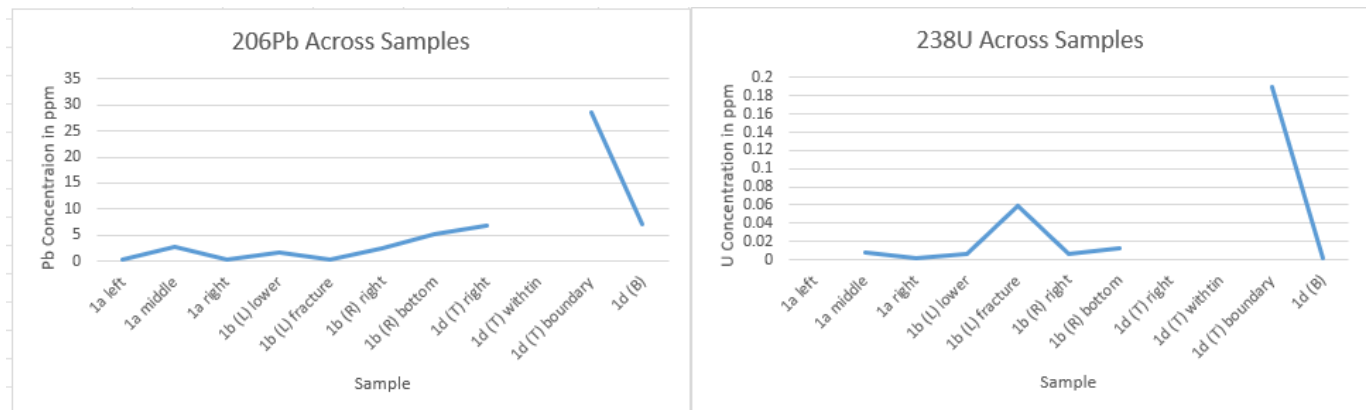


Fig. 24 Plots of ²⁰⁶Pb and ²³⁸U across all samples (except sample 3a, which had extremely dissimilar values).

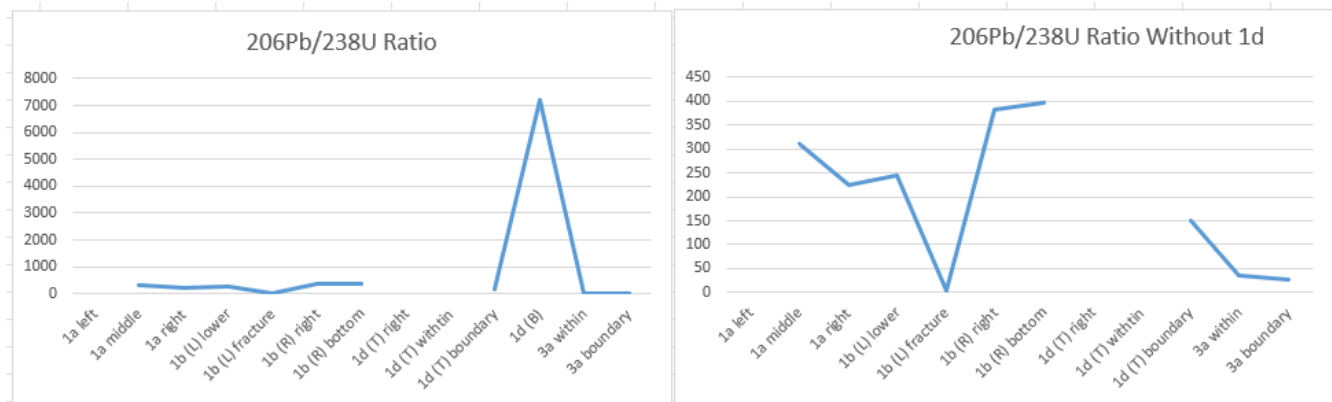


Fig. 25 Ratios of $^{206}\text{Pb}/^{238}\text{U}$ for all samples (left), and all samples without the bottom site of sample 1d (right).

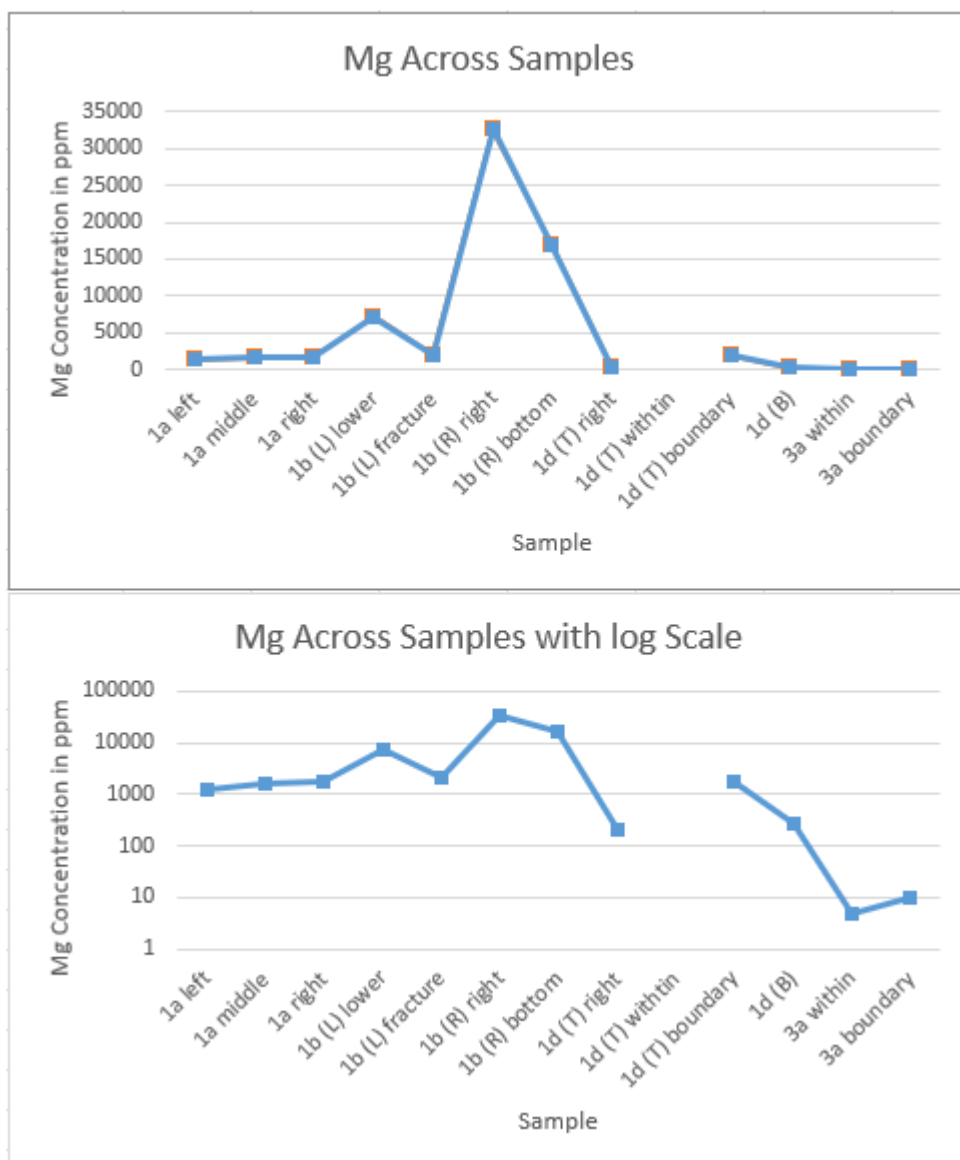


Fig. 26 Graphs visualizing Mg across all samples, one graph with a linear scale on the Y axis (top) and one graph with a log scale on the Y axis (bottom).

Figures 17-21 show REE (Rare Earth Element) trends for different zones of each sample. Overall, REE trends are somewhat out of the expected trend for calcite, which should generally follow normal trends.

Sample 1a (figure 17) seems to have a very large positive anomaly in Ho in the left section of the ablation site, and overall, an enrichment in HREEs (Heavy Rare Earth Elements) throughout the site, with also a slight enrichment of La and Ce on the left and right sides, but not the center, of the site.

Sample 1b (figures 18 and 19) shows a large positive Eu anomaly in all areas except the upper section of the left site. All sections with a positive Eu anomaly in sample 1b are within the green portion of the amygdule, and the clear/white portion contains the negative Eu anomaly. The green portion of the amygdule also exhibits an enrichment in LREEs (Light Rare Earth Elements), especially La, while the clear/white portion is enriched in HREEs and LREEs towards the extremes of either side, forming somewhat of a V shape on the graph (if you exclude the relatively low Ce content).

Data from sample 1d (figure 20) was unfortunately mostly unusable. There were many negative values exported from Iolite, which lead to many holes in the trend line, and some sets that could not form trend lines at all. The one useable set from the center of the bottom site of sample 1d does exhibit a somewhat normal REE trend (normal in the sense that it is closer to expected), with an enrichment in LREEs and a positive anomaly in Er and Lu, leading to a taper at the right side of the graph.

Sample 3a (figure 21) is the calcite vein, rather than an amygdule, and exhibits another somewhat more normal REE trend with an enrichment in HREEs in the section of just the vein, the values for La and Ce are also somewhat high. In the section that included some of the surrounding basalt, the trend line creates a very smooth bowl like pattern, with a negative anomaly in La, a positive anomaly in Ce, and an enrichment in HREEs.

The graphs shown for REE trends in this section were created from data in the non-Int2SE table, found Appendix A, figure II.

In figure 22, the right section of the right site of sample 1b seems to contain outlying data point for both Ce and Yb. The bottom section of the right site of sample 1b also exhibits a larger concentration of Ce and Yb than the rest of the samples. This could represent some sort of inclusion within this part of the amygdule, or because this site is within the green section of calcite for sample 1b, this could suggest differing concentrations throughout the green section of calcite in sample 1b. Other than the right site of sample 1b, samples seem to sit between 1-10 ppm of both Ce and Yb. The ratio between the two isotopes exhibits an odd zigzag patter, but this is partially to do with the positioning of the samples relative to each other, but also with the upper section of the left site of sample 1b (labelled “fracture” on these graphs). This section is within the clear/white section of the amygdule, while the green section exhibits a much higher ratio.

In figure 23, concentrations of Sr and Ba are displayed. A similar pattern for sample 1b can be seen in the Sr plot, but not in the Ba plot. Interesting to see is a decrease in Sr for sample 1a from left to right, and relatively no change from left to right for Ba in the same sample. The Ba concentrations in total are relatively flat, with most samples being in the 1-10 ppm range, and some reaching 20-30. The one outlier is the “boundary” section for the top section of sample 1d (this is the section on the edge of the inner section, encompassing both the inner and out section of the top site of sample 1d). The Sr/Ba ratios also exhibit an odd zig-zag pattern, both between and within samples. Sample 1a has a much lower ratio in the middle section, and very high ratios on both the left and right section. In general, the average is around 100 for the ratio value, but 1a left and right, and 1b fracture have much higher ratios, and sample 1d top and bottom, and sample 3a have much lower Sr/Ba ratios.

For Mg plots, the right site on sample 1b exhibits much higher Mg concentrations than other samples. The lower section of the left site of sample 1b also exhibits slightly higher Mg concentrations than other samples. All of these sections are in the green section of calcite for sample 1b, and the lowest Mg concentration is within the clear/white section of

calcite in sample 1b. Sample 1a exhibits concentrations between 1200-1800ppm, increasing from left to right. Sample 1d has concentrations under 1000ppm, except for the boundary section of the top site. Sample 3a has the lowest Mg concentrations, with values under 10ppm.

Discussion

Eu^{2+} will commonly replace Ca^{2+} in many different systems, and that is true of calcite as well. We can see that in sample 1b, both left and right sites, the REE graph shows a large positive Eu anomaly in all inspected sections except for the upper section of the left site. All of the sections that display this large positive Eu anomaly are within the green parts of sample 1b, suggesting this area had much more replacement of Ca with Eu. The upper section of the right site of sample 1b is within the clear/white section of the amygdule, and has a negative Eu anomaly. This negative suggests less replacement, or perhaps less Ca to have been replaced. It could also suggest Eu diffusion into the green growth of the crystal, if the green section grew after the clear/white section of the amygdule. The positive Eu anomalies also seem to correlate with positive Ce anomalies, which is interpreted to be an interference within the REEs. There is, however, possibility of the Ce anomalies being from inclusions present in the samples. The same goes for the Ho anomaly in sample 1a, this is most likely an interference with the slight possibility of an inclusion.

Partitioning for REEs in calcite⁸ lets us interpret that samples and sections enriched in LREEs likely grew in earlier stages of calcite growth than those enriched in HREEs. Early calcite growth will partition LREEs out of the solution, enriching earlier growths in LREEs. It is likely that HREE enriched sections and samples grew later. Sample 3a is perhaps an exception, as it is a vein rather than an amygdule. The veins are interpreted to have grown during the Acadian Orogeny, rather than the eruption event, and so is from a different system of fluid, and this may be the reason the bowl-like pattern is visible for that sample. The green section of sample 1b (all sections within 1b other than the “upper” section) all exhibit enrichment in LREEs, suggesting earlier growth. The opposite is true for the upper

section of the left site of sample 1b. The middle and right sections of sample 1a exhibit enrichment in HREEs, suggesting later growth, while the left side displays the large Ho anomaly and slight HREE enrichment.

HREE enrichment could also have come from later seawater intrusion⁸, potentially during the Acadian Orogeny and the vein formation, and some samples with known alteration⁶ exhibit higher HREE content in them.

Sample 1a seems to have trends moving left to right on the ablation site from the graphs seen (figures 22-26). This suggests some growth difference from the left to right side for sample 1a, Sr in sample 1a we can see that the growth was faster on the right side of the sample (from higher Sr content).

Mg content generally corresponds to growth temperature, with higher Mg content equalling higher temperature growth. Looking at the Mg concentration graphs, we can assume that sample 1b, specifically the green section of sample 1b, probably grew at greater temperatures than the white section of sample 1b, and at greater temperatures than other samples. Temperatures overall were shown to be centered around $\sim 350^{\circ}\text{C}$, and $\sim 200^{\circ}\text{C}$ in Helmke 2024⁶, and the Mg content graphs would relate the green section of sample 1b to this higher $\sim 350^{\circ}\text{C}$ growth phase. Closer to the center of the green section, the right side of the right site of sample 1b exhibits the highest Mg concentration, and could be close to the core of the growth for the green section.

U and Pb were put into a ratio of Pb/U to be used in a Terra-Wasserburg concordia plot for age calculation. Unfortunately, across all samples both Pb and U concentrations are very low. U is under 0.01ppm in all samples, except sample 3a which sits around 4ppm and 10ppm for the vein and the vein/basalt boundary. Such low U content makes acquiring an age for the samples difficult without further spot analysis and lower detection limits on the instruments used. We can see, however, that sample 1d has a very high ratio. This comes from higher Pb content, and a very low U concentration.

Conclusion

From this project we can understand the REE distribution across the four samples studied, as well as other trace element contexts and Mg concentrations for these samples. A little more is known about the potential growth history of these samples as well. Sample 1b has a more complex structure than before thought, and exhibits different patterns of growth and REE distribution across the amygdule, both within and between the clear/white and green sections of the amygdule.

Time constraints on the project limited abilities to collect data and do analysis. In the future, analysis could be repeated using solid standards^{11, 12} rather than just general powdered standards, for more accurate results. Temperature maps could be made with Mg data to determine exactly the higher temperature zones in the amygdules, and spot analysis with lower detection limits for ^{238}U could be done to acquire more accurate ^{238}U data. This could be used in tandem with similar Pb analysis, and the more accurate carbonate standards, to obtain better data for more accurate age calculations. This could be done as a future project, or as an extension of this project.

In my opinion, sample 1b should be studied more closely, as it exhibits interesting patterns both between the clear/white section and the green section, and within the green section, in all analyses performed. The difference between clear/white section and green section growth could be studied more, and age calculations could be done separately for each section of sample 1b.

References

1. Edward Anders, Nicolas Grevesse, Abundances of the elements: Meteoritic and solar, *Geochimica et Cosmochimica Acta*, Volume 53, Issue 1, 1989, Pages 197-214,
- 2 . J. B. Murphy, J. D. Keppie and A. J. Hynes, 1991. DP ME 188, Version 1, 2006. Digital Version of Geological Survey of Canada Map 1749A, Geology, Antigonish Highlands, Nova Scotia, parts of NTS 11E/07, 11E/08, 11E/09, 11E/10, 11E/16, and 11F/13, scale 1:50 000
3. Murphy, J. B. (2001). Geochemistry, provenance, and tectonic significance of sedimentary rocks of the Middle to Late Devonian McArras Brook and Visean Martin Road formations, Merigomish Subbasin, northern Antigonish Highlands, Nova Scotia. *Atlantic Geology*, 37(2/3), 161–173. <https://doi.org/10.4138/1977>
4. Andjić, G., Zhou, R., Buchs, D.M. *et al.* Paleozoic ocean plate stratigraphy unraveled by calcite U-Pb dating of basalt and biostratigraphy. *Commun Earth Environ* **3**, 113 (2022). <https://doi.org/10.1038/s43247-022-00446-1>
5. Rembe, J., Zhou, R., Sobel, E. R., Kley, J., Chen, J., Zhao, J.-X., Feng, Y., and Howard, D. L.: Calcite U–Pb dating of altered ancient oceanic crust in the North Pamir, Central Asia, *Geochronology*, 4, 227–250, <https://doi.org/10.5194/gchron-4-227-2022>, (2022).
6. Helmke, I.: Characterization of Calcite Amygdules in Devonian Basalts, in the McArras Brook Formation, Nova Scotia, Dalhousie University, (2024).

7. L. M. Anovitz, E. J. Essene, Phase Equilibria in the System $\text{CaCO}_3\text{-MgCO}_3\text{-FeCO}_3$, *Journal of Petrology*, Volume 28, Issue 2, April 1987, Pages 389-415, <https://doi.org/10.1093/petrology/28.2.389>
8. Mucci, Alfonso. "Partitioning of Rare Earth Elements (REEs) between Calcite and Seawater Solutions at 25°C and 1 Atm, and High Dissolved REE Concentrations." *Geochimica Et Cosmochimica Acta*, 1995.
9. Petrus, J.A., Chew, D.M., Leybourne, M.I. and Kamber, B.S. (2017) A new approach to laser-ablation inductively-coupled-plasma mass-spectrometry (LA-ICP-MS) using the flexible map interrogation tool ?Monocle?. *Chemical Geology* 463, p. 76-93.
10. Paton, C., Hellstrom, J., Paul, B., Woodhead, J. and Hergt, J. (2011) Lolite: Freeware for the visualisation and processing of mass spectrometric data. *Journal of Analytical Atomic Spectrometry*. doi:10.1039/c1ja10172b.
11. Roberts, N. M. W., E. Troy Rasbury, R. R. Parrish, C. J. Smith, M. S. A. Horstwood, and D. J. Condon (2017), A calcite reference material for LA-ICP-MS U-Pb geochronology, *Geochem. Geophys. Geosyst.*, 18, 2807–2814, doi:[10.1002/2016GC006784](https://doi.org/10.1002/2016GC006784).
12. Rasbury, E. T., Present, T. M., Northrup, P., Tappero, R. V., Lanzirotti, A., Cole, J. M., Wootton, K. M., and Hatton, K.: Tools for uranium characterization in carbonate samples: case studies of natural U–Pb geochronology reference materials, *Geochronology*, 3, 103–122, <https://doi.org/10.5194/gchron-3-103-2021>, 2021.

Appendix A

Sample	1a left	1a middle 1a right	1b (left) lower	1b (left) fracture	1b (right) middle right 1b (right) middle bottom	1d (top) right 1d (top) within	1d (top) boundary	1d bottom big center	no basal	basalt
									3a left	3a right edge
La	1.860936	0.134186	0.419499	1.22650707	1.078926385	8.398106213	6.313603519	3.948843131	9.0299604	3.961700226
Ge	4.718492	0.805046	1.252305	5.519973759	1.339376756	26.5737372	18.5825911	10.01683586	8.82063236	124.0766
Pr	0.256811	0.060576	0.080047	0.343543091	0.241623229	2.913257966	1.803963325	0.79732546	0.681210961	1.81205063
Nd	1.129208	0.487672	0.467786	1.523099403	1.318952436	11.9630161	7.607204818	6.298120157	5.487116	4.339950515
Sm	0.023374	0.093963	0.094283	0.345262099	0.281305674	1.301569302	1.666689583	1.18522877	0.390900929	1.3928729
Eu	0.118687	0.059787	0.060457	0.248514054	0.080207558	1.114037956	1.114037956	1.114037956	1.114037956	1.114037956
Gd	0.427041	0.261839	0.200774	0.407491084	0.349962153	3.209533554	1.936911488	2.012374729	1.653954778	19.83371
Dy	0.907404	0.434428	0.31891	0.453968778	0.661836591	2.379397574	1.861150031	1.72.79096236	1.835790053	25.1781
Ho	1.52602	0.1931	0.12862	0.111196325	0.179441014	0.665754578	0.416208678	0.416208678	0.416208678	0.609107
Er	0.81065	0.463749	0.35419	0.420715929	0.588575528	2.060389618	1.224685809	2.524738473	1.530754926	21.20716
Tm		0.14759	0.073844	0.064283957	0.03937982	0.297370433	0.178464298		0.16870587	3.040424
Yb	1.1415	0.620068	0.438518	0.443174133	0.66550037	2.012607755	1.260341036	1.171745883	23.72308	53.54236
Lu	0.281217	0.163487	0.099906	0.073571588	0.11224082	0.349582446	0.21547025	0.840072398	0.218219093	3.586106
Sample	1a left	1a middle 1a right	1b (left) lower	1b (left) fracture	1b (right) middle right 1b (right) middle bottom	1d (top) right 1d (top) within	1d (top) boundary	1d bottom big center	no basal	basalt
									3a left	3a right edge
La	0.154301	0.057175	0.033535	0.107111044	0.072111319	0.343479123	0.254886123	0.17033549	1559.71424	6.658375453
Ge	0.310674	0.136534	0.101585	0.319814983	0.23086113	1.1169277	0.957965258	0.397860906	4.0172021	0.942144634
Pr	0.017547	0.007986	0.010338	0.031063279	0.018612809	0.135942648	0.083455998	0.041568933	78.5426541	0.335426259
Nd	0.081045	0.043713	0.08041	0.140556484	0.11049791	0.543621483	0.017323541	0.259872072	31.07162574	0.800177431
Sm	0.024917	0.015383	0.020868	0.041050378	0.038891795	0.171604859	0.094739285	0.059957358	159.9514379	0.679262833
Eu	0.001064	0.007112	0.012908	0.0010664	0.007112	0.012908	0.00158822	0.02186406	11.7555872	1.468187879
Gd	0.042666	0.027968	0.063247	0.04267878	0.050851829	0.1862671256	0.104935768	0.079555668	12892.4167	2.139384249
Dy	0.096714	0.031484	0.082106	0.042946073	0.056217858	0.171102475	0.094332201	1.032747374	3192.21927	2.822545635
Ho	0.300533	0.012145	0.034	0.0979749405	0.04777084	0.092202628	0.213232951	43.6381083	3.113902181	0.014080093
Er	0.00505	0.030701	0.067111	0.030502782	0.04773444	0.110409389	0.05893897	185.1519136	0.322467156	0.24837
Tm	0.732002	0.0077485	0.030041	0.026666161	0.008912927	0.017889172	0.009328154	3.7872095	3.211691209	0.05090334
Yb	0.104464	0.03849	0.09315	0.038476191	0.057939365	0.116593125	0.06049265	0.646848914	116.053472	1.56407872
Lu	0.026319	0.008983	0.01207	0.009918096	0.011170224	0.020975965	0.010675603	2.204759098	1.637614021	2.277357352
									0.00725807	0.2987819
									12.921116	9.281291
									53.54236	1.875312

Fig. I Reduced and un-normalized REE data, bottom set is Int2SE values from lolite, top set is non-Int2SE values.

Sample	1a left	1a middle 1a right	1b (left) lower	1b (left) fracture	1b (right) middle right 1b (right) middle bottom	1d (top) right 1d (top) within	1d (top) boundary	1d bottom big center	no basalt	basalt			
									3a left edge	3a right edge			
La	0.657439	0.243611	0.142885	0.456374281	0.307248144	1.463841564	1.086008194	0.725758372	6645.566007	28.36972924	0.74473617	15.39652	34.90572
Ce	0.515042	0.22635	0.168409	0.60600272	0.382727338	1.851669586	1.090791211	0.659583731	68.30523907	1.561910865	0.530063046	15.4065	52.1597
Pr	0.196935	0.089628	0.116032	0.348633883	0.208958579	1.525731177	0.936655417	0.46654246	881.3092302	3.767029129	0.640819698	14.59525	34.21429
Nd	0.179145	0.096626	0.17741	0.31069725	0.244254213	1.201638999	0.825012702	0.574429868	68.681745	1.76873875	0.320069686	13.23519	24.75062
Sm	0.16939	0.107971	0.190812	0.27960442	0.264390176	1.166586398	0.644046803	0.40759895	108491.8	4.617697367	0.394570031	12.21422	36.91152
Eu	0.19043	0.127003	0.230501	0.500988617	0.179327083	1.416043085	0.717212815	0.431900112	209.9212604	26.21764069	0.285209949	10.90918	26.00603
Gd	0.217017	0.14726	0.321703	0.220188976	0.25065304	0.928927949	0.533752611	0.498634856	65780.34966	11.45891317	0.312163	9.31163	28.73817
Dy	0.396491	0.129728	0.33802	0.176929021	0.231635178	0.704993778	0.38867821	0.425542581	12934.56681	11.62977188	0.25389992	10.1133	33.142
Er		0.236421	0.61115	0.175349014	0.264876619	0.59525214	0.376263807	3.835125022	784.8595636	56.00543491	0.252329074	11.59436	49.58354
Ho	0.434743	0.193211	0.423604	0.220407567	0.208394062	0.69477908	0.224669646	11652.10281	2.028939482	0.2947177	16.2546	66.02672	
Tm		0.324175	1.241373	0.273332285	0.36830275	0.739220022	0.385460897	0.978042642	6354.84384	13.540595	0.243940258	15.49104	59.21369
Yb	0.643975	0.236861	0.57326	0.236776585	0.335654994	0.717268924	3.981441161	7.17451212	9.625099865	0.223015256	18.38762	79.51485	
Lu	1.083088	0.365689	1.111539	0.28469529	0.45967999	0.863208425	0.439232543	90.73066	67.39152352	9.731408956	0.298460415	18.60623	77.17335
Sample	1a left	1a middle 1a right	1b (left) lower	1b (left) fracture	1b (right) middle right 1b (right) middle bottom	1d (top) right 1d (top) within	1d (top) boundary	1d bottom big center	no basalt	basalt			
La	7.929898	0.571733	1.787382	5.225859321	4.588525158	35.78203172	26.9003972	16.8250666	38.47581118	16.879984758	222.9704	247.05	
Ce	7.824344	1.344626	2.076103	9.151103011	8.220452181	44.05399687	30.8115899	15.27004429	10.84707191	16.60610625	14.62377857	205.6972	323.0285
Pr	2.875022	0.679862	0.96539	3.855702479	3.717881363	32.696516	20.24650197	10.97567392	7.645465327	12.80813763	189.0001	200.5846	
Nd	2.561954	1.077966	1.360739	3.36670876	2.917445703	26.34744828	16.83215843	13.92157418	12.12893063	5.953170899	148.3919	174.4834	
Sm	1.51852	0.636932	0.64193	2.34712508	1.912342316	20.50095379	11.46614264	8.07996325	2.657382113	4.946662069	117.5938	153.366	
Eu	2.119388	1.069264	1.079583	4.24991932	4.132277813	24.360841	19.8217526	8.696312555	269.2874859	7.426768361	117.762	142.421	
Gd	2.172131	1.331834	1.02123	2.07269168	2.541309872	16.32520424	9.852043173	10.2365597		8.40268103	99.6802	153.5714	
Dy	3.738787	1.789599	1.012037	2.035380625	2.73253438	13.5124149	6.70172281	93.92780781		52.62036409	13.7417	177.8907	
Ho	27.464461	3.478913	2.313301	1.99993961	3.22756573	12.06638216	7.48576794			7.886035599	109.1566	207.5204	
Tm	5.104637	2.918496	2.229012	2.64677336	3.79406249	12.96658035	7.707273812	29.755536		15.88885131	133.4621	272.516	
Yb		6.098754	3.051389	2.65636185	3.85867028	12.38803441	7.54557761			19.47328521	125.796	250.594	
Lu	7.024615	3.8158	2.698571	2.77225344	4.01846383	12.38527849	7.755944838			6.87478494	145.9882	329.497	
	11.57271	6.727875	4.111342	3.027637364	4.618993796	14.22977027	8.867088492	34.57088056		5.98020968	147.5764	333.5638	

Fig. II Normalized REE data, top set is Int2SE values and bottom set is non-Int2SE values.

Appendix B

Sample 1a			
Name	Left Side	Right Side	Middle
Area (μm^2)	301990.21	211127	52303.812
Points	678	474	129
Type	Polygon	Polygon	Polygon
X (μm)	165.24853	1323	812.58259
Y (μm)	496.88969	221.75	439.06898
Sr88_ppm	1137.7261	575.24	488.66163
Sr88_ppm Int2SE	47.387013	38.19	29.652232
Ba137_ppm	1.7067602	6.4853	0.9067926
Ba137_ppm Int2SE	0.112228	1.0606	0.3076866
La139_ppm	1.8609357	0.4195	0.1341858
La139_ppm Int2SE	0.1543009	0.0572	0.0335351
Ce140_ppm	4.7184922	1.2523	0.8050464
Ce140_ppm Int2SE	0.3106736	0.1365	0.1015845
Pr141_ppm	0.2561805	0.086	0.0605757
Pr141_ppm Int2SE	0.0175469	0.008	0.0103385
Nd146_ppm	1.1590281	0.4678	0.487672
Nd146_ppm Int2SE	0.0810453	0.0437	0.0804103
Sm147_ppm	0.2233743	0.0944	0.0936928
Sm147_ppm Int2SE	0.0249173	0.0159	0.0280684
Eu153_ppm	0.1186829	0.0605	0.0598788
Eu153_ppm Int2SE	0.0106641	0.0071	0.012908
Gd157_ppm	0.4270411	0.2008	0.2618385
Gd157_ppm Int2SE	0.0426656	0.028	0.0632468
Dy163_ppm	0.9074035	0.3189	0.4344278
Dy163_ppm Int2SE	0.0967138	0.0315	0.0821059
Ho165_ppm	1.5260204	0.1286	0.1930995
Ho165_ppm Int2SE	0.3005307	0.0131	0.0340002
Er166_ppm	0.8109647	0.3542	0.4637489
Er166_ppm Int2SE	0.0690791	0.0307	0.0673107
Tm169_ppm		0.0738	0.1475898
Tm169_ppm Int2SE	0.7320022	0.0078	0.0300412
Yb172_ppm	1.1414999	0.4385	0.6200676
Yb172_ppm Int2SE	0.104646	0.0385	0.0931548
Lu175_ppm	0.2812168	0.0999	0.1634874
Lu175_ppm Int2SE	0.026319	0.009	0.0270104
Pb204_ppm	0.6750603	2.4795	-0.115235
Pb204_ppm Int2SE	0.6395281	0.8023	1.6718343
Pb206_ppm	0.3606585	2.6377	0.3315493
Pb206_ppm Int2SE	0.0791885	0.4306	0.1483992
Pb207_ppm	0.4531692	3.4522	0.6843186
Pb207_ppm Int2SE	0.0789921	0.5211	0.2903897
Pb208_ppm		12.715	
Pb208_ppm Int2SE	0.2376459	6.042	0.1553015
Th232_ppm		0.0002	
Th232_ppm Int2SE	2.857E-06	0.0005	2.496E-17
Mg24_ppm	1237.1944	1600.5	1720.3558
Mg24_ppm Int2SE	43.761958	62.735	63.884582
U238_ppm		0.0085	0.0014732
U238_ppm Int2SE	0.0094615	0.0031	0.0029888
PbTotal_ppm	0.3368819	2.3165	0.3690328
PbTotal_ppm Int2SE	0.0564115	0.3247	0.1515064

Fig. I Data table exported from Iolite V4 for sample 1a.

Sample 1b left					
Name	Lower Zo	Fracture	Total Lead	and U Interest	
Area (μm ²)	79836	49203	65395		
Points	583	369	462		
Type	Polygon	Polygon	Polygon		
X (μm)	320.25	816.42	577.91		
Y (μm)	446.62	242.47	394.02		
PbTotal_ppm	1.6821	0.2597	1.1013		
PbTotal_ppm Int2S	0.389	0.0705	0.2823		
Mg24_ppm	7176.2	2035.9	1978.5		
Mg24_ppm Int2SE	1763	89.264	120.29		
Sr88_ppm	209.46	36.788	123.19		
Sr88_ppm Int2SE	16.792	1.5924	15.256		
Ba137_ppm	2.7404	0.0823	1.3747		
Ba137_ppm Int2SE	0.5051	0.0198	0.2811		
La139_ppm	1.2265	1.0769	0.825		
La139_ppm Int2SE	0.1071	0.0721	0.0447		
Ce140_ppm	5.52	1.3394	2.8979		
Ce140_ppm Int2SE	0.3981	0.2309	0.3136		
Pr141_ppm	0.3435	0.2422	0.2264		
Pr141_ppm Int2SE	0.0311	0.0186	0.0147		
Nd146_ppm	1.5231	1.3199	1.1421		
Nd146_ppm Int2SE	0.1406	0.1105	0.0828		
Sm147_ppm	0.3453	0.2813	0.2478		
Sm147_ppm Int2SE	0.0411	0.0389	0.0307		
Eu153_ppm	0.2405	0.0802	0.1462		
Eu153_ppm Int2SE	0.0281	0.01	0.0172		
Gd157_ppm	0.4075	0.4996	0.3947		
Gd157_ppm Int2SE	0.0433	0.0509	0.0426		
Dy163_ppm	0.494	0.6632	0.5459		
Dy163_ppm Int2SE	0.0429	0.0562	0.0452		
Ho165_ppm	0.1112	0.1794	0.1347		
Ho165_ppm Int2SE	0.0097	0.0147	0.0118		
Er166_ppm	0.4207	0.5886	0.4761		
Er166_ppm Int2SE	0.035	0.0477	0.0404		
Tm169_ppm	0.0643	0.0934	0.0675		
Tm169_ppm Int2SE	0.0066	0.0089	0.0072		
Yb172_ppm	0.4432	0.6666	0.506		
Yb172_ppm Int2SE	0.0385	0.0579	0.0415		
Lu175_ppm	0.0736	0.1122	0.0874		
Lu175_ppm Int2SE	0.0069	0.0112	0.0083		
Pb204_ppm	2.9729	0.8225	1.9985		
Pb204_ppm Int2SE	0.653	0.5417	0.564		
Pb206_ppm	1.7216	0.1639	1.352		
Pb206_ppm Int2SE	0.4143	0.0349	0.3807		
Pb207_ppm	1.9677	0.1762	1.1989		
Pb207_ppm Int2SE	0.4901	0.0472	0.3135		
Pb208_ppm	1.5942	0.2545	0.8982		
Pb208_ppm Int2SE	0.3674	0.0773	0.2234		
Th232_ppm	0.0046	0.0119	0.0081		
Th232_ppm Int2SE	0.0015	0.0029	0.0022		
U238_ppm	0.007	0.059	0.0273		

Fig. II Data table exported from lolite V4 for the left site of sample 1b.

Sample 1b right		
Name	Middle Ri	Middle Bottom
Area (μm²)	166028	296467
Points	693	1238
Type	Polygon	Polygon
X (μm)	1718	1189.6
Y (μm)	500.2	775.19
Sr88_ppm	1217.4	940.72
Sr88_ppm Int2SE	47.224	29.635
Ba137_ppm	10.997	10.788
Ba137_ppm Int2SE	0.6135	0.973
La139_ppm	8.3981	6.3136
La139_ppm Int2SE	0.3435	0.2549
Ce140_ppm	26.573	18.585
Ce140_ppm Int2SE	1.1169	0.658
Pr141_ppm	2.9133	1.804
Pr141_ppm Int2SE	0.1359	0.0835
Nd146_ppm	11.96	7.6072
Nd146_ppm Int2SE	0.5436	0.3732
Sm147_ppm	3.0157	1.6867
Sm147_ppm Int2SE	0.1716	0.0947
Eu153_ppm	1.3642	1.11
Eu153_ppm Int2SE	0.0793	0.0402
Gd157_ppm	3.2095	1.9369
Gd157_ppm Int2SE	0.1826	0.1049
Dy163_ppm	3.2794	1.8616
Dy163_ppm Int2SE	0.1711	0.0943
Ho165_ppm	0.6676	0.4162
Ho165_ppm Int2SE	0.0331	0.0209
Er166_ppm	2.0604	1.2247
Er166_ppm Int2SE	0.1104	0.059
Tm169_ppm	0.2974	0.1785
Tm169_ppm Int2SE	0.0179	0.0093
Yb172_ppm	2.0126	1.2603
Yb172_ppm Int2SE	0.1166	0.0605
Lu175_ppm	0.3458	0.2155
Lu175_ppm Int2SE	0.021	0.0107
Pb204_ppm	5.4542	7.6648
Pb204_ppm Int2SE	1.4219	1.3107
Pb206_ppm	2.3593	5.0595
Pb206_ppm Int2SE	0.4904	0.5531
Pb207_ppm	1.7456	4.2097
Pb207_ppm Int2SE	0.2588	0.399
Pb208_ppm	1.6588	5.4005
Pb208_ppm Int2SE	0.2406	0.6078
Th232_ppm	0.0024	0.0008
Th232_ppm Int2SE	0.0011	0.0004
Mg24_ppm	32643	16755
Mg24_ppm Int2SE	3816.8	1792.2
U238_ppm	0.0062	0.0127
U238_ppm Int2SE	0.002	0.002
PbTotal_ppm	1.8879	5.4782

Fig. III Data table exported from Iolite V4 for the right site of sample 1b.

Sample 1d top			
Name	Right Sid	Within	Boundary
Area (μm²)	81822	62178	86211
Points	801	606	873
Type	Polygon	Polygon	Polygon
X (μm)	1283.8	645.96	712.02
Y (μm)	332.68	755.53	393.6
Sr88_ppm	181.6		190.19
Sr88_ppm Int2	10.481	41109	42.831
Ba137_ppm	22.419		197.95
Ba137_ppm In	2.2057	18094	82.865
La139_ppm	3.9488		9.03
La139_ppm In	0.1703	1559.7	6.6584
Ce140_ppm	9.2111	6.543	10.017
Ce140_ppm In	0.3979	41.202	0.9421
Pr141_ppm	0.9779		0.6812
Pr141_ppm Int2	0.0416	78.525	0.3356
Nd146_ppm	6.2981		5.4871
Nd146_ppm In	0.2599	31.072	0.8002
Sm147_ppm	1.1885		0.3909
Sm147_ppm In	0.06	15959	0.6793
Eu153_ppm	0.487	15.08	
Eu153_ppm In	0.0242	11.756	1.4682
Gd157_ppm	2.0125		
Gd157_ppm In	0.098	12932	2.1938
Dy163_ppm	22.796		12.771
Dy163_ppm In	1.0327	3139.2	2.8225
Ho165_ppm			
Ho165_ppm In	0.2132	43.638	3.1139
Er166_ppm	4.6519		2.5247
Er166_ppm Int2	0.1946	1851.5	0.3224
Tm169_ppm			
Tm169_ppm In	0.0237	153.79	3.2317
Yb172_ppm			
Yb172_ppm In	0.647	116.05	1.5641
Lu175_ppm		0.8401	
Lu175_ppm In	2.2048	1.6376	2.2774
Pb204_ppm	5.5187		
Pb204_ppm In	1.0038	534437	1061.9
Pb206_ppm	6.8301		28.674
Pb206_ppm In	0.4989	16570	13.309
Pb207_ppm	11.012		27.234
Pb207_ppm In	0.8965	16316	10.181
Pb208_ppm			
Pb208_ppm In	0.3216	44013	11.214
Th232_ppm		14809	
Th232_ppm In	0.0098	33424	189099
Mg24_ppm	207.78		1846.7
Mg24_ppm Int2	8.7667	93230	959.49
U238_ppm			0.1895
U238_ppm Int2	0.3723	1268.3	0.3161
PbTotal_ppm	7.1699		
PbTotal_ppm	0.5306	16567	272.05

Fig. IV Data table exported from Iolite V4 for the top site of sample 1d.

Sample 1d bottom	
Name	Big Center
Area (μm²)	302092.53
Points	1270
Type	Polygon
X (μm)	823.89601
Y (μm)	387.06584
Sr88_ppm	167.51668
Sr88_ppm Int2SE	6.6355136
Ba137_ppm	33.577333
Ba137_ppm Int2SE	3.8669814
La139_ppm	3.9617002
La139_ppm Int2SE	0.1747896
Ce140_ppm	8.8210632
Ce140_ppm Int2SE	0.319734
Pr141_ppm	1.1412051
Pr141_ppm Int2SE	0.057037
Nd146_ppm	4.3399505
Nd146_ppm Int2SE	0.1447995
Sm147_ppm	1.3929873
Sm147_ppm Int2S	0.0580413
Eu153_ppm	0.415899
Eu153_ppm Int2SE	0.0159718
Gd157_ppm	1.6519547
Gd157_ppm Int2Si	0.065053
Dy163_ppm	1.8357901
Dy163_ppm Int2SE	0.0616191
Ho165_ppm	0.4384636
Ho165_ppm Int2Si	0.0140801
Er166_ppm	1.5307549
Er166_ppm Int2SE	0.0468297
Tm169_ppm	0.1687086
Tm169_ppm Int2Si	0.0059034
Yb172_ppm	1.1171459
Yb172_ppm Int2SE	0.0362426
Lu175_ppm	0.2182191
Lu175_ppm Int2SE	0.0072528
Pb204_ppm	6.7156712
Pb204_ppm Int2S	0.9158085
Pb206_ppm	7.0518982
Pb206_ppm Int2S	0.3963222
Pb207_ppm	8.0806001
Pb207_ppm Int2S	0.4377005
Pb208_ppm	7.0578293
Pb208_ppm Int2S	0.3730711
Th232_ppm	
Th232_ppm Int2Si	3.458E-05
Mg24_ppm	272.66098
Mg24_ppm Int2SE	11.241703
U238_ppm	0.0009751
U238_ppm Int2SE	0.0003855
PbTotal_ppm	6.9205154
PbTotal_ppm Int2S	0.359423

Fig. V Data table exported from Iolite V4 for the bottom site of sample 1d.

Sample 3a			
Name	Left Edge	Right Edge	With Basalt
Area (μm^2)	141711.6	150001	
Points	770	808	
Type	Polygon	Polygon	
X (μm)	514.9119	1187.7	
Y (μm)	438.2491	653.36	
Sr88_ppm	10655.12	9484.1	
Sr88_ppm lr	1010.984	1171.4	
Ba137_ppm	3939.824	4287.6	
Ba137_ppm	368.8365	752.89	
La139_ppm	52.33114	57.983	
La139_ppm	3.613564	8.1924	
Ce140_ppm	124.0766	194.88	
Ce140_ppm	9.293198	31.484	
Pr141_ppm	16.83391	17.872	
Pr141_ppm lr	1.300437	3.0485	
Nd146_ppm	67.13248	78.936	
Nd146_ppm	5.575314	11.197	
Sm147_ppm	17.29805	22.557	
Sm147_ppm	1.796712	5.4297	
Eu153_ppm	6.594962	7.9756	
Eu153_ppm	0.610914	1.4563	
Gd157_ppm	19.65371	30.182	
Gd157_ppm	1.830771	5.6499	
Dy163_ppm	25.1781	43.174	
Dy163_ppm	2.454501	8.1892	
Ho165_ppm	6.069107	11.538	
Ho165_ppm	0.644646	2.7568	
Er166_ppm	21.20716	43.305	
Er166_ppm lr	2.5833	10.492	
Tm169_ppm	3.044204	6.0644	
Tm169_ppm	0.374883	1.433	
Yb172_ppm	23.72308	53.543	
Yb172_ppm	2.987989	12.921	
Lu175_ppm	3.586106	8.1056	
Lu175_ppm	0.452131	1.8753	
Mg24_ppm	313001.6	436955	
Mg24_ppm lr	28375.36	70261	
Pb204_ppm		6074.4	
Pb204_ppm	4382.763	8593.2	
Pb206_ppm	176.8066	272.49	
Pb206_ppm	15.5177	38.978	
Pb207_ppm	202.8277	314.56	
Pb207_ppm	18.38439	45.464	
Pb208_ppm	193.6089	282.18	
Pb208_ppm	17.24613	40.2	
U238_ppm	4.821769	10.082	
U238_ppm lr	0.561923	2.3696	
PbTotal_ppm	200.5808	315.5	
PbTotal_ppm	17.61789	45.257	
Th232_ppm	18.18842	38.74	
Th232_ppm	2.149311	8.5493	

Fig. VI Data table exported from Iolite V4 for sample 3a.

Appendix C

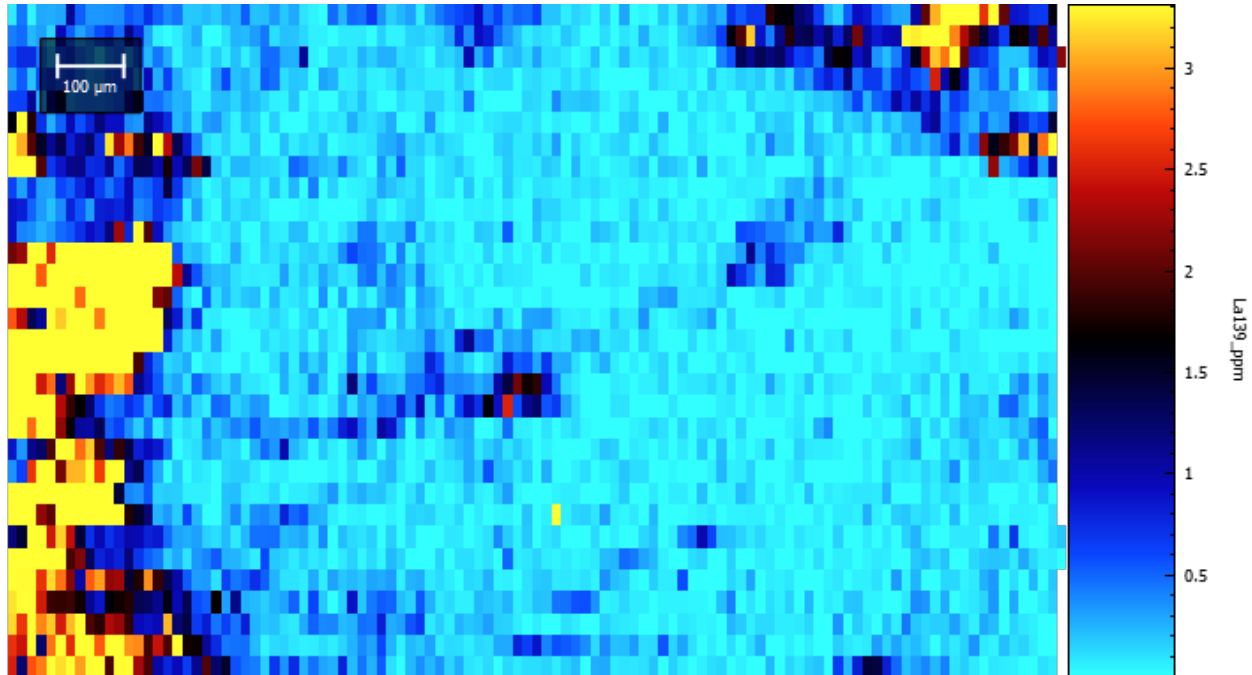


Fig. I La distribution in sample 1a.

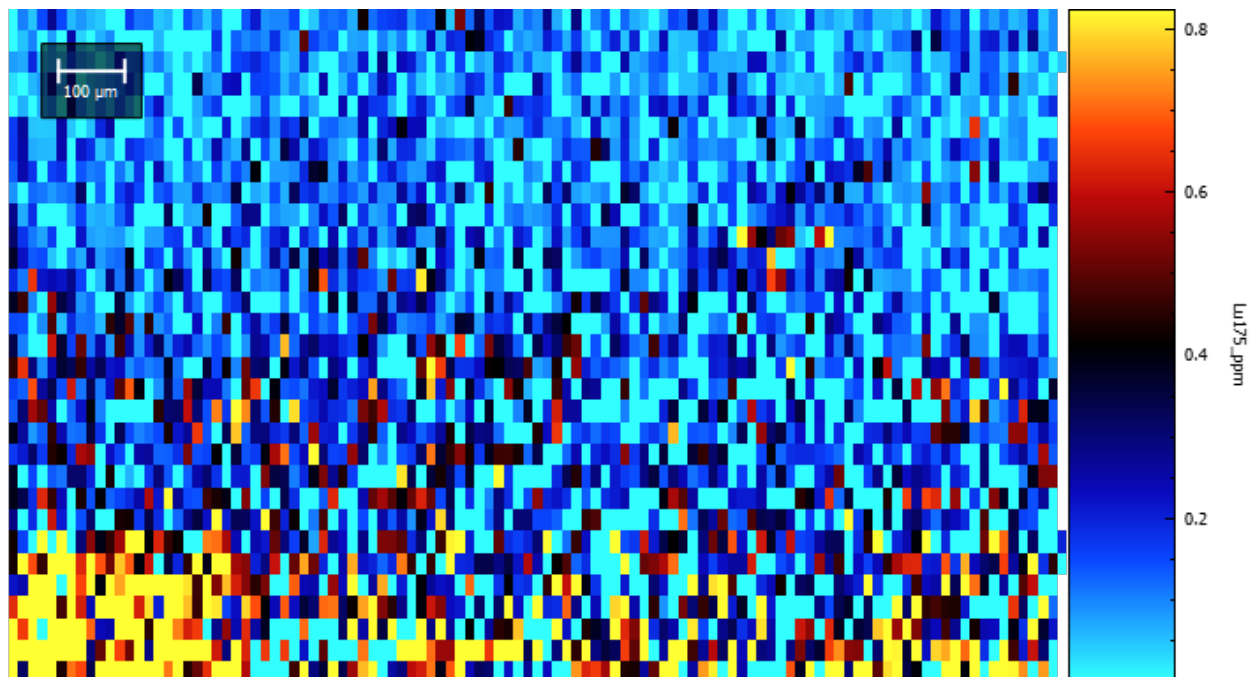


Fig. II Eu distribution in sample 1a.

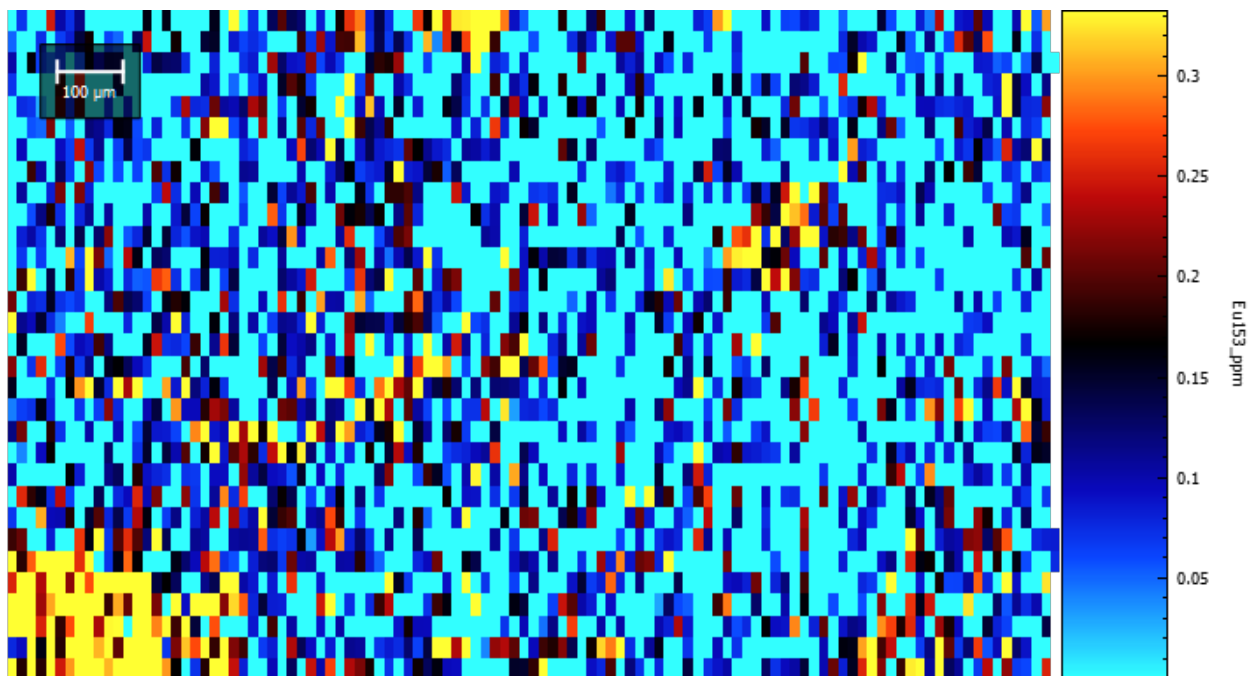


Fig. III Lu distribution in sample 1a.

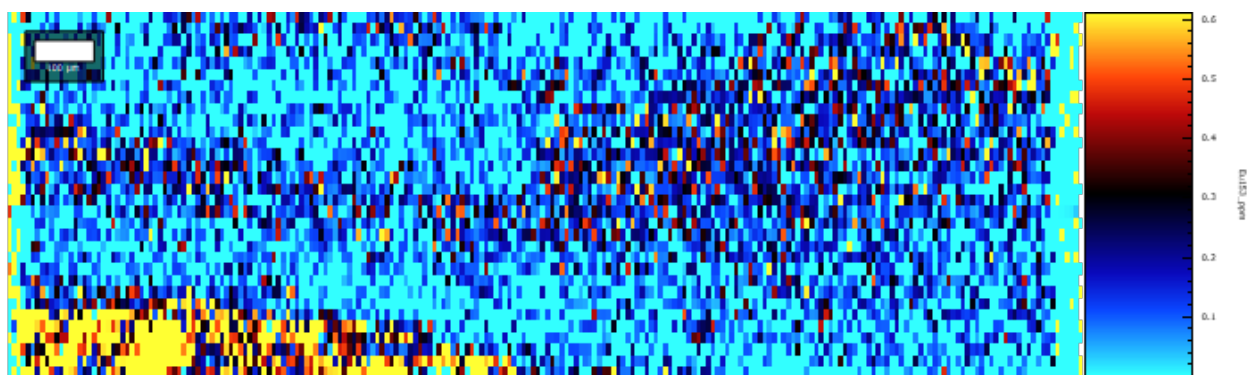


Fig. IV Eu distribution in the left site of sample 1b.

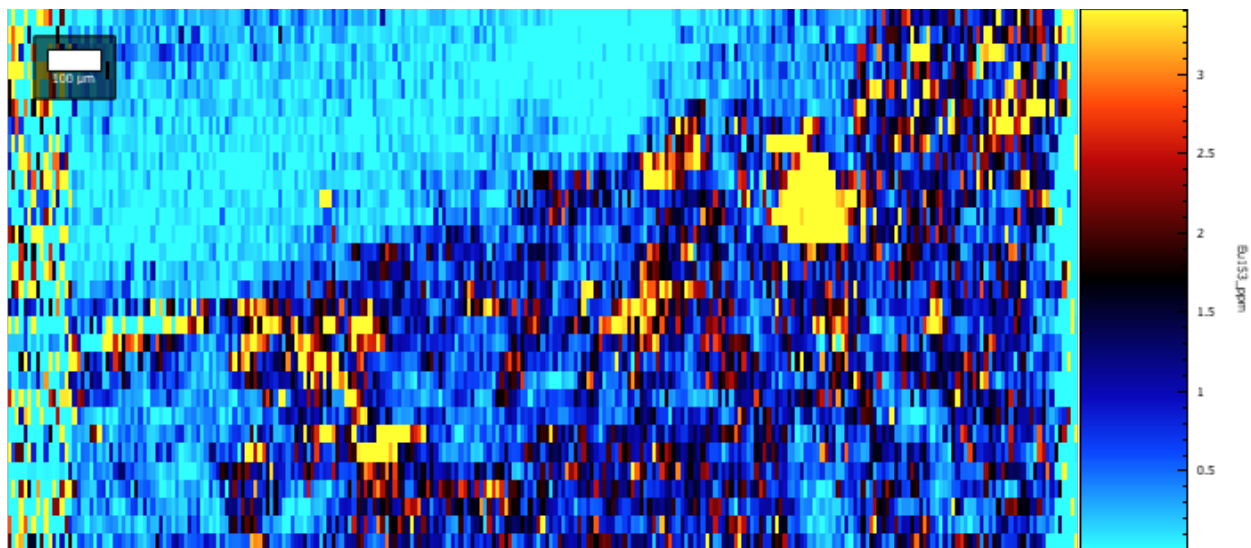


Fig. V Eu distribution in the right site of sample 1b.

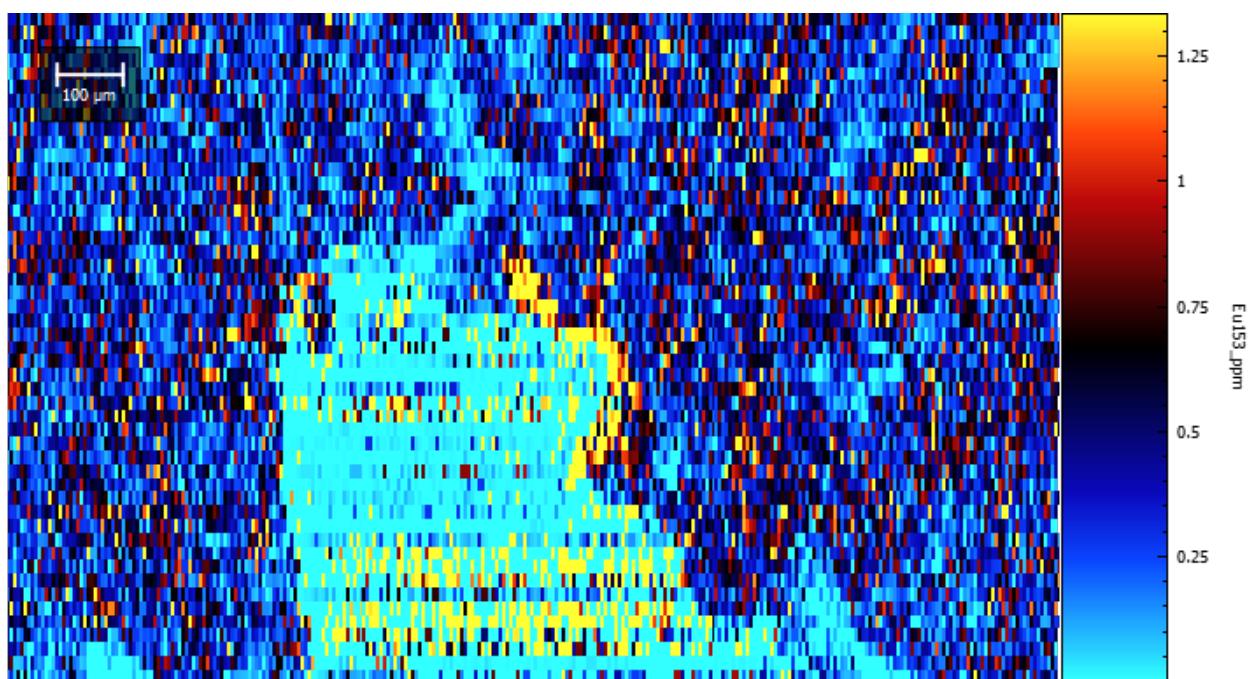


Fig. VI Eu distribution in the top site of sample 1d.

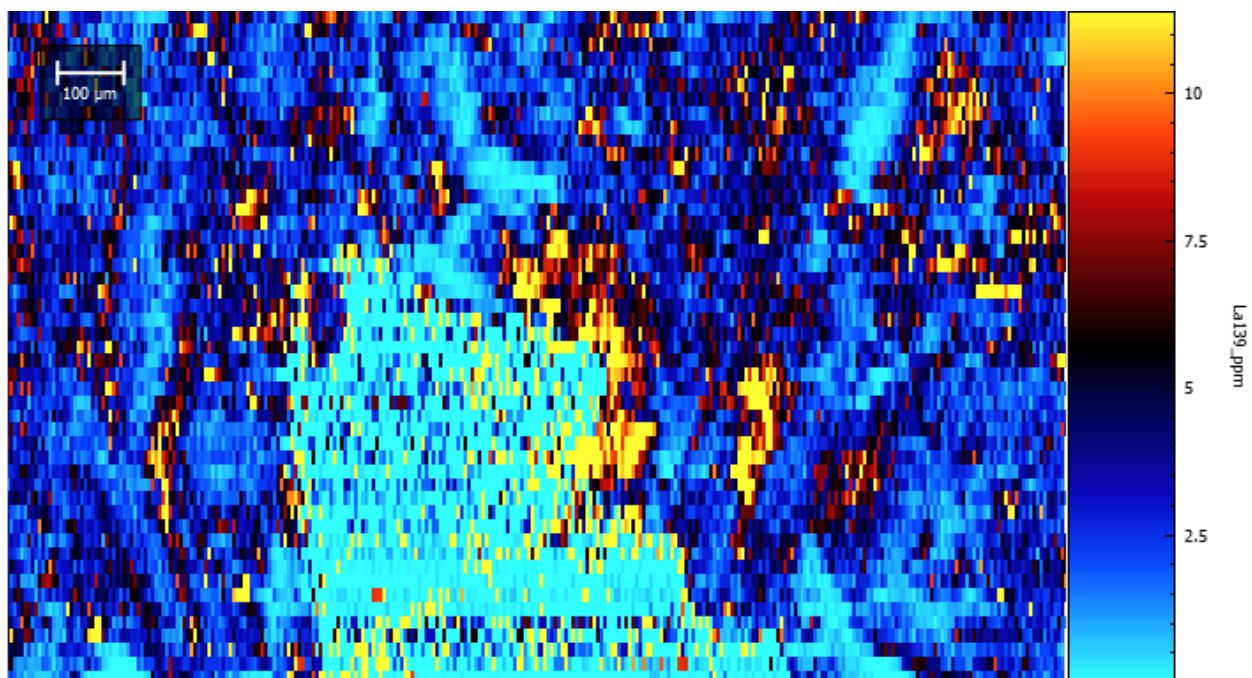


Fig. VII La distribution in the top site of sample 1d.

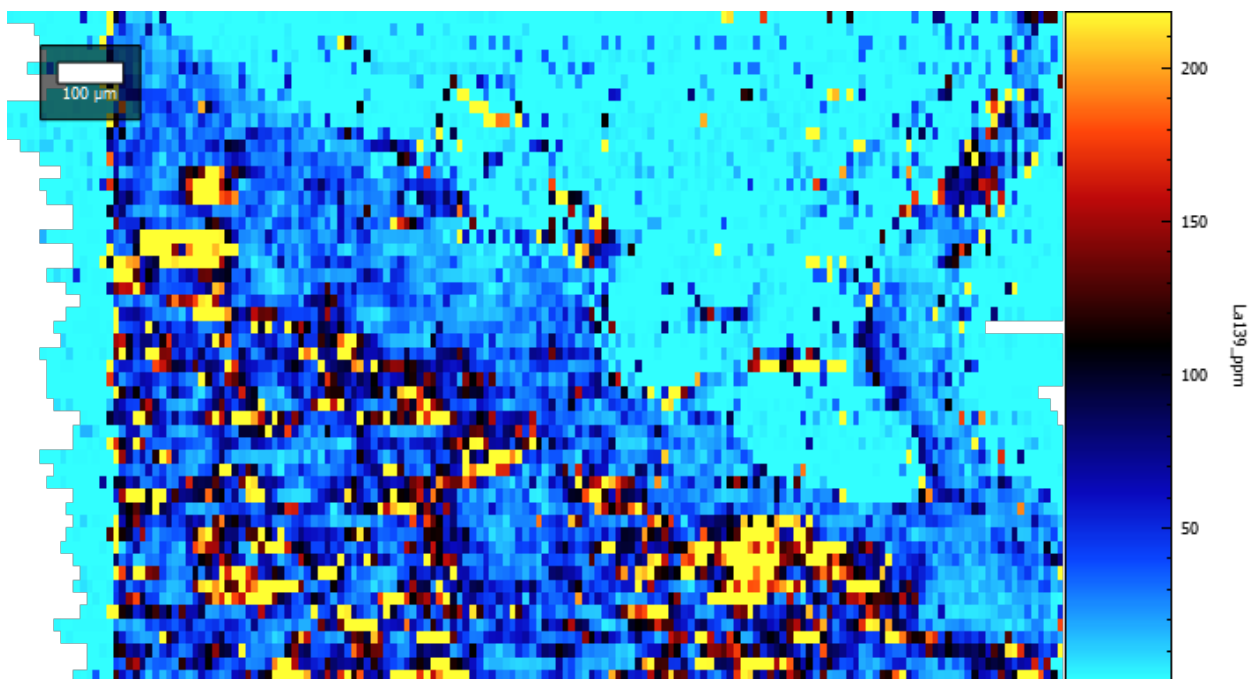


Fig. VIII La distribution in sample 3a.

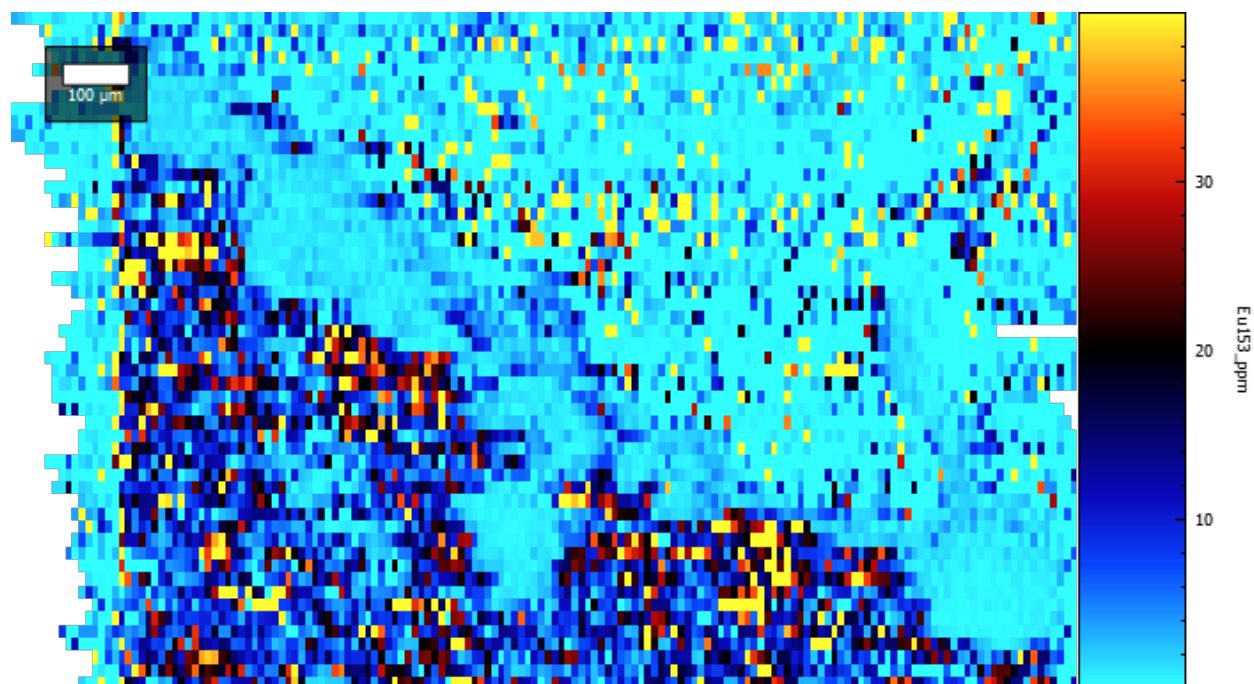


Fig. IX Eu distribution in sample 3a.